frontiers | Frontiers in Earth Science

TYPE Original Research
PUBLISHED 23 June 2023
DOI 10.3389/feart.2023.1197363

OPEN ACCESS

EDITED BY
Dmitri Rouwet,
Istituto Nazionale di Geofisica e Vulcanologia, Italy

REVIEWED BY
Gino Gonzalez,
University of Bari Aldo Moro, Italy
Peter Kelly,
United States Geological Survey (USGS), United States

*CORRESPONDENCE
Manuel Inostroza,
manuelinostrozap@gmail.com

RECEIVED 30 March 2023
ACCEPTED 06 June 2023
PUBLISHED 23 June 2023

CITATION
Inostroza M, Fernandez B, Aguilera F, Layana S, Walter TR, Zimmer M, Rodríguez-Díaz A and Oelze M (2023), Physical and chemical characteristics of active sulfur flows observed at Lastarria volcano (northern Chile) in January 2019. *Front. Earth Sci.* 11:1197363. doi: 10.3389/feart.2023.1197363

Physical and chemical characteristics of active sulfur flows observed at Lastarria volcano (northern Chile) in January 2019

Manuel Inostroza[1]*, Bárbara Fernandez[2], Felipe Aguilera[1,2], Susana Layana[1], Thomas R. Walter[3], Martin Zimmer[3], Augusto Rodríguez-Díaz[4] and Marcus Oelze[3,5]

[1]Millennium Institute on Volcanic Risk Research—Ckelar Volcanoes, Antofagasta, Chile, [2]Departamento de Ciencias Geológicas, Universidad Católica del Norte, Antofagasta, Chile, [3]GFZ German Research Centre for Geosciences, Potsdam, Germany, [4]Alcaldía Coyoacán, Instituto de Geofísica, Universidad Nacional Autónoma de México, Mexico City, Mexico, [5]Bundesanstalt für Materialforschung und—prüfung (BAM), Berlin, Germany

Molten sulfur is found in various subaerial volcanoes. However, limited records of the pools and flows of molten sulfur have been reported: therefore, questions remain regarding the physicochemical processes behind this phenomenon. A suite of new sulfur flows, some of which active, was identified at the Lastarria volcano (northern Chile) and studied using satellite imagery, *in situ* probing, and temperature and video recording. This finding provides a unique opportunity to better understand the emplacement mechanisms and mineral and chemical compositions of molten sulfur, in addition to gaining insight into its origin. Molten sulfur presented temperatures of 124–158°C, with the most prolonged sulfur flow reaching 12 m from the source. Photogrammetric tools permitted the identification of levees and channel structures, with an estimated average flow speed of 0.069 m/s. Field measurements yielded a total volume of 1.45 ± 0.29 m^3 of sulfur (equivalent to ~2.07 tons) mobilized during the January 2019 event for at least 408 min. Solidified sulfur was composed of native sulfur with minor galena and arsenic- and iodine-bearing minerals. Trace element analysis indicated substantial enrichment of Bi, Sb, Sn, Cd, as well as a very high concentration of As (>40.000 ppm). The January 2019 molten sulfur manifestations in Lastarria appear to be more enriched in As compared to the worldwide known volcanoes with molten sulfur records, such as the Shiretoko-Iozan and Poás volcanoes. Furthermore, their rheological properties suggest that the "time of activity" in events such as this could be underestimated as flows in Lastarria have moved significantly slower than previously thought. The origin of molten sulfur is ascribed to the favorable S-rich chemistry of fumarolic gases and changes in host rock permeability (fracture opening). Molten sulfur in Lastarria correlates with a peak in activity characterized by high emissions of SO_2 and other acid species, such as HF and HCl, in addition to ground deformation. Consequently, molten sulfur was framed within a period of volcanic unrest in Lastarria, triggered by changes in the magmatic-hydrothermal system. The appearance of molten sulfur is related to physicochemical perturbations inside the volcanic system and is perhaps a precursor of eruptive activity, as observed in the Poás and Turrialba volcanoes.

KEYWORDS
sulfur flows, sulfur pools, molten sulfur, arsenic, Lastarria

1 Introduction

Native sulfur is a common constituent of Earth's volcanoes and is found in the solid phase within fumarolic deposits in response to persistent fumarolic activity. Although native sulfur is highly abundant in fumarolic deposits, few volcanoes have evidence of molten sulfur, being a very "exotic" feature and, consuently, a target of interest for several studies (e.g., Wanatabe and Shimotomai, 1937; Oppenheimer and Stevenson, 1989; Greeley et al., 1990; Oppenheimer, 1992; Harris et al., 2004). Sulfur is the element with the largest number of allotropes (at least 30 different crystal structures in the solid phase), forming rings and unbranched chains of stable or metastable sulfur according to the temperature-pressure cooling conditions (Meyer, 1976; Steudel and Eckert, 2003). Each allotrope has a melting point (e.g., Steudel and Eckert, 2003). For natural molten sulfur, cooling leads to pure α–and β–sulfur regardless of the liquid temperature, with approximate liquidus temperatures of 115 and 120 °C (Meyer, 1976; Steudel and Eckert, 2003), respectively. Accordingly, the temperature and viscosity of molten sulfur are strongly correlated, influencing the rheological properties and morphologies of quenched flows (e.g., MacKnight and Tobolsky, 1965; Theiling, 1982). For example, once molten, sulfur reaches a minimum viscosity at ~159 °C, then increases up to four orders of magnitude at 160 °C due to the polymerization of its molecules. As a result, yellowish tones predominate at temperatures lower than 120°C while orange shades prevail in the 120–160°C range, varying to reddish shades at temperatures of 160–250°C. Finally, at temperatures >250°C, sulfur presents dark brown to black shades (MacKnight and Tobolsky, 1965; Meyer, 1976; Theiling, 1982; Oppenheimer and Stevenson, 1989; Ikehata et al., 2019; Mora-Amador et al., 2019; Inostroza et al., 2020).

Evidence of past natural molten sulfur is currently observed as fossil sulfur flows, such as in Mauna Loa in Hawaii (Skinner, 1970; Greeley et al., 1984), Galapagos Island (Colony and Nordlie, 1973), and Momotombo volcano, Nicaragua (Smithsonian Institution, 1990), which preserve pahoehoe, lobe-like, or leeve morphologies (e.g., Wanatabe, 1940; Skinner, 1970; Naranjo, 1985; Mora-Amador et al., 2019). Further evidence of subaerial sulfur flows has also been found at Lastarria volcano, where Naranjo (1985; Naranjo, 1988) described a 350-m-long sulfur flow. Other Andean volcanoes with evidence of fossil sulfur flows in their fumarolic deposits include Tacora, Guallatiri, Irruputuncu, Aucalquincha, Ollagüe, and Bayo (Leiding, 1936; Rodríguez, 1962; Naranjo, 1988; Aguilera, 2008; Inostroza et al., 2020).

Active sulfur flows have rarely been witnessed and were observed for the first time in 1936 at the Shiretoko-Iozan volcano (Japan), where a 1,400 m-long flow was emitted (Wanatabe, 1940). More recently, in January 2012, González et al. (2015) noted active sulfur flows (up to 175 m) at the Turrialba volcano. Molten sulfur has also been observed directly related to the aqueous phase in crater lakes as sulfur spherules, such as in the case of Poás volcano, Costa Rica (Bennett and Raccichini, 1978; Oppenheimer and Stevenson, 1989; Oppenheimer, 1992; Mora-Amador et al., 2019), Kusatsu-Shirane, Japan (Takano and Watanuki, 1990) and Copahue, Argentina-Chile (Delpino and Bermúdez, 1993; Delpino and Bermúdez, 1993; Daga et al., 2017), among others, where the hydrothermal system scrubs the S-bearing compounds. Additionally, molten sulfur has been observed at the Daikoku submarine volcano (Mariana arc, Embley et al., 2007; de Ronde et al., 2015), indicating the varied types of subaerial and underwater environments in which these molten sulfur manifestations can occur.

One of the main features of molten sulfur is its reddish-to-orange appearance. This feature has been observed when the sulfur temperature is above 200°C. However, reddish molten sulfur was found in the Poás and Hakone volcanoes at temperatures of 116–159°C (Oppenheimer and Stevenson, 1989; Ikehata et al., 2019). Kargel et al. (1999) suggested that the different colors of molten sulfur could also be related to impurities (e.g., As, Cl, I, and H_2S) within, impacting the melt viscosity and its rheological behavior. Other studies have reported significant concentrations of As, Au, Mo, Ni, and Pb in solidified sulfur flows (Oppenheimer and Stevenson, 1989; Kargel et al., 1999; Daga et al., 2017), which play important roles in modifying the rheological properties (Bacon and Fanelli, 1943; Matsushima and Ono, 1959; Rubero, 1964; Touro and Wiewiorowski, 1966; Scolamacchia and Cronin, 2016). Molybdenum, W, Bi, Hg, Au, and Cu can also be enriched in molten sulfur but at lower concentrations than those of the elements mentioned above (Skinner, 1970).

The formation of molten sulfur is usually attributed to the melting and remobilization of fumarolic deposits previously formed by the changes in the thermal gradient or the opening of new vents within the fumarolic field (Colony and Nordlie, 1973; Meyer, 1976; Naranjo, 1985). Nevertheless, it was later established that the reactions between the sulfur species (SO_2 and H_2S) and H_2O are also responsible for the formation of liquid sulfur, especially in emissions where the outlet temperature of gases is below ~400°C (Giggenbach, 1987; Oppenheimer, 1992; Takano et al., 1994; Delmelle et al., 2000). Independently of the process behind molten sulfur formation, previous studies have effectively shown that sulfur deposition is thermodynamically more efficient at temperatures below 200°C and atmospheric pressure (Giggenbach and Matsuo, 1991). In the same manner, the presence of water at temperatures between ~100 and 350°C (i.e., in the hydrothermal reservoir or the base-vent of crater lakes) catalyzes the formation of sulfur (Delmelle and Bernard, 2015).

Molten sulfur can be regarded as a phenomenon that occurs in specific volcanoes with limited bibliographic records. This phenomenon is important because molten sulfur has been observed prior to or during eruptive events, mainly of a phreatic nature, suggesting a potential correlation with volcanic unrest (e.g., González et al., 2015; Daga et al., 2017; Salvage et al., 2018; Mora-Amador et al., 2019). In January 2019, active pools and flows of molten sulfur were observed and described scientifically for the first time at the Lastarria volcano in northern Chile (Figure 1A), a volcano affected by ground deformation (e.g., Pritchard and Simonds, 2002; Henderson et al., 2017) and changes in the chemical composition of volcanic gases (López et al., 2018; Layana et al., 2023). This phenomenon offers a unique opportunity to investigate the rheological, mineral, and chemical properties of these materials.

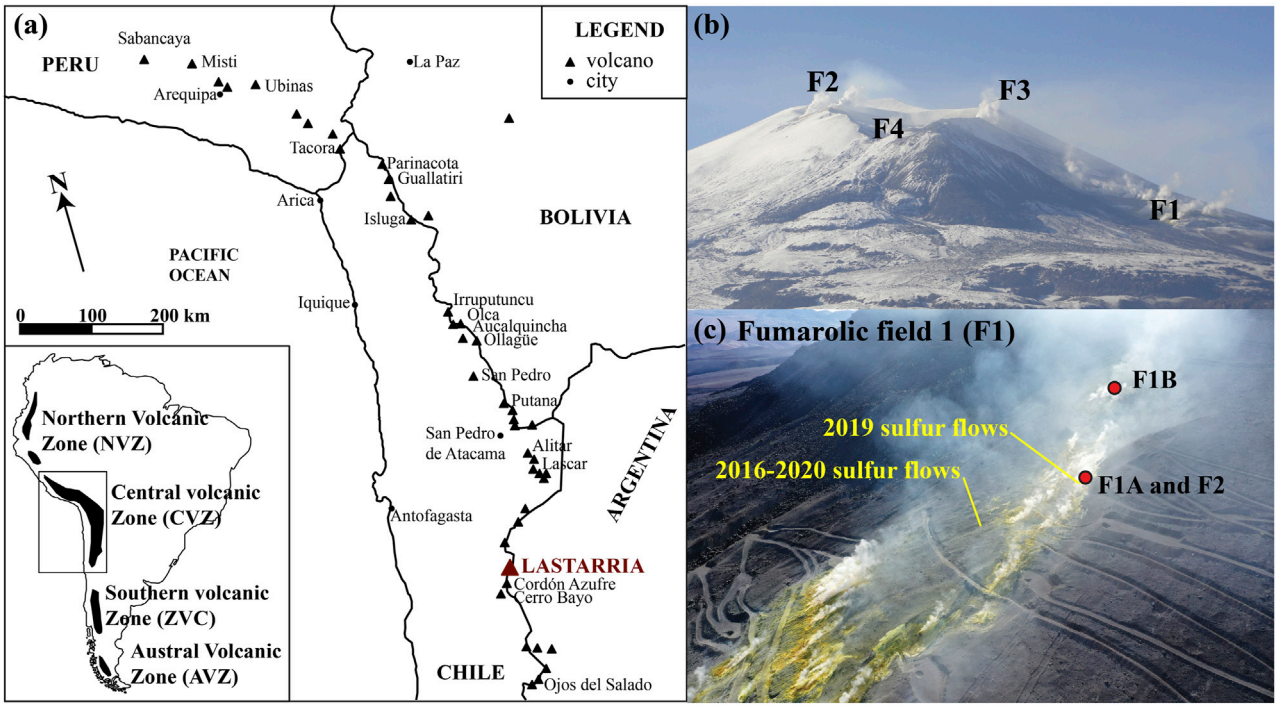

FIGURE 1
(A) Location map of the Central Volcanic Zone (CVZ) of the Andes, including the Northern, Southern, and Austral Volcanic Zones (NVZ, SVZ, and AVZ, respectively), showing the Lastarria volcano as a red triangle. **(B)** General view of the northern side of Lastarria volcano, including the four fumarolic fields (F1-F4). **(C)** Drone photographs of the fumarolic field 1 (F1), showing the location of the 2019 sulfur flows (samples F1A and F2; coordinate 25.1552°S, 68.5213°W), a pool of molten sulfur in the upper part of the fumarolic field 1 (sample F1B; coordinate 25.1556°S, 68.5194°W), and undocumented sulfur flows accounted between 2016 and 2020 (further details in Figure 2). Further drone photographs in Fig. S2.1. Coordinates in UTM-WGS-84. For scale, consider bulldozer roads that are 3–4 m wide.

Later, in April 2019 and February 2020, the site was revisited, and new solidified sulfur flows were described and investigated. In this study, we present *in situ* measurements (emission and emplacement temperatures, as well as the length, width, and thickness of the flows), video and photographic captures, and mineralogical and chemical analyses of molten sulfur samples with the aim of i) constraining the emplacement mechanisms of the sulfur flows and pools, ii) determining their chemical and mineral characteristics, and iii) evaluating the possible origin of molten sulfur manifestations. Moreover, this study provides insights into the occurrence of sulfur flows and the ongoing unrest affecting Lastarria volcano.

2 Geological background

The Lastarria Volcanic Complex (LVC) belongs to the Lazufre volcanic area, along with Cordón del Azufre and Bayo volcanoes (Pritchard and Simons, 2002). The LVC is formed by the Lastarria volcano (the site referred to in this study), the Negriales lava field, and the Espolón volcano. The LVC was built over Upper Miocene–Lower Pleistocene andesitic-to-dacitic lava flows and domes beneath Lower Pleistocene dacitic ignimbrites (Naranjo and Cornejo, 1992). The volcanic edifice comprises basaltic andesites to dacitic lava flows and domes, in addition to block and ash and fallout deposits. Its geological evolution has been divided into 10 eruptive stages, with ages ranging from 260 ± 20 to <2.45 ± 50 ka (Naranjo, 2010). Furthermore, this volcano has recorded two avalanche deposits on its SE flank (Naranjo and Francis, 1987; Rodriguez et al., 2020).

In recent decades (1997–2016), Interferometric Synthetic Aperture Radar (InSAR) images have detected continuous ground deformation in the Lazufre area, reaching inflation rates of up to ~3 cm/yr (Pritchard and Simons, 2002, Pritchard and Simons, 2004; Froger et al., 2007; Ruch et al., 2008; Henderson et al., 2017). This inflation has been attributed to magmatic and hydrothermal fluids circulating beneath the volcano at different depths, and is related to two deformation sources: the deeper source at 7–15 km below the volcano summit, ascribed to magmatic intrusion, and the shallower source located at a depth of ~1 km, corresponding to an overpressurized hydrothermal system (Froger et al., 2007; Spica et al., 2015). The inflation rate, related to deeper sources, decreased to approximately 1.5 cm/yr in mid-2016 (Henderson et al., 2017). Currently, no updated geodetic information is available for this deformation episode. However, frequency-magnitude analysis of long-period and volcano-tectonic events collected in 2011–2013 suggest episodic magmatic and hydrothermal activity, in which hypocenters are located within 15 km below the volcano summit (McFarlin et al., 2022).

Persistent and vigorous fumarolic activity indicates magmatic and hydrothermal fluids feeding surface emissions, placing Lastarria as one of the most important gas suppliers within the last decade of northern Chilean volcanoes, with typical SO_2 fluxes approximately

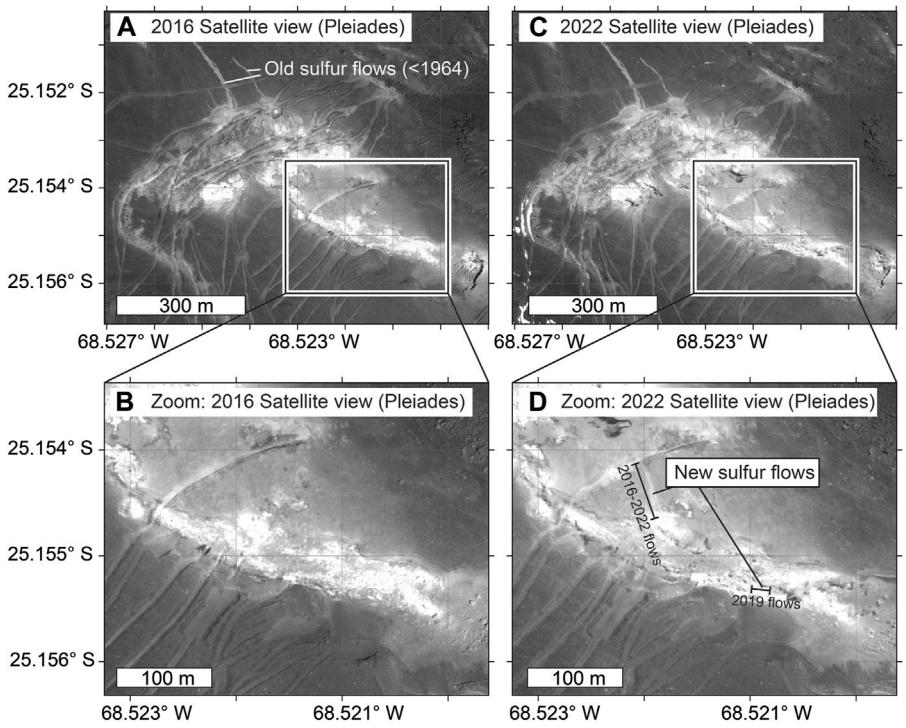

FIGURE 2
Remote sensing reveals sulfur flows on the fumarolic field 1, which occurred on an undetermined date between 2016 and 2022 (2016–2022 flows) and January 2019 (2019 flows). The upper row is the overview map, and the lower row is the close-view **(A, B)** 2016 Pleiades image shows the presence of old sulfur flows and the fumarole field as bright pixels **(C, D)** 2022 Pleiades image shows new sulfur flows as bright pixel flow-like structures. Panel **(D)** shows the position of the 2016–2022 and 2019-flows, which emerged at 5,100 and 5,114 m above sea level, respectively. The latter was recorded and presented in Figs. 3 and 4, and Supplementary Material S1.

800 t/d (Tamburello et al., 2014; Layana et al., 2023). Gas discharges reach temperatures of up to 408°C, emitting considerable amounts of acid magmatic species, such as SO_2, HCl, and HF, in addition to hydrothermal-related species, such as H_2S and CH_4 (Aguilera et al., 2012). Magmatic emissions most likely originate from at least two magma chambers located at depths of 3–6 and 7–15 km, respectively, whereas hydrothermal emissions correlate well with the presence of a hydrothermal reservoir at a depth <1 km below the summit (Froger et al., 2007; Aguilera et al., 2012; Spica et al., 2015; Robidoux et al., 2020; Layana et al., 2023). According to Aguilera et al. (2012), variable scrubbing within the volcanic edifice explains temperature variations and fluctuating contributions of magmatic and hydrothermal compounds to fumarolic emissions. The hydrothermal system comprises a discontinuous hydrothermal aquifer fed with condensed steam and occasional meteoric water inputs. Since late 2012, the chemical composition of the discharged gases has evolved into a more magmatic signature (Tamburello et al., 2014; Lopez et al., 2018; Layana et al., 2023), likely owing to the acidification of the hydrothermal system triggered by a substantial input of volatiles from a pressurized and volatile-rich magma chamber (Layana et al., 2023).

As a product of fumarolic activity, vast yellow crusts and alteration zones, the so-called fumarolic deposits, were mainly deposited on the northern flank of the volcano (Figure 1B). These areas are formed by the desublimation and condensation of gas compounds, covering rock surfaces and producing a great variety of fumarolic minerals (e.g., Africano and Bernard, 2000; Balić-Žunić et al., 2016). Fumarolic deposits at the Lastarria volcano present variable colors (e.g., white, yellowish, orange, reddish, and gray) as a function of the outlet temperature and chemistry of the fumarolic gases (Aguilera et al., 2016; Inostroza et al., 2020). Sulfates and sulfides, along with minor halides, borates, and native elements, dominated the mineral assemblage. These fumarolic deposits are remarkable for the presence of As-, Pb-, and Tl-bearing minerals, in addition to significant concentrations of other metals, such as Se, Cd, Zn, and Cu (Aguilera et al., 2016; Inostroza et al., 2020). However, the main feature of the Lastarria fumarolic deposits is the presence of 220–350-m-long sulfur flows (Naranjo, 1985, Naranjo, 1988) that were active prior to 1964, according to old aerial photographs (Figure 2A). They preserve rope-like morphologies, a pale yellowish color, and many lithic fragments. The physical and rheological properties of sulfur suggest emplacement under low-temperature -viscosity conditions (Naranjo, 1988).

3 Field observations, recording, sampling, and analytical procedures

3.1 Field observations and recording

Satellite images were acquired before and after the emplacement of the sulfur flows in 2019 (Figure 2), and

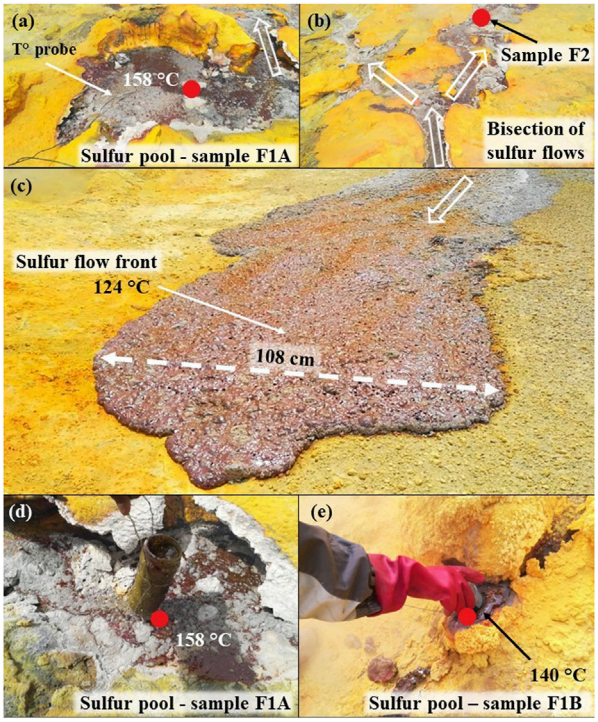

FIGURE 3
Pool and flows of molten sulfur observed in January 2019 at Lastarria volcano. **(A)** A molten sulfur pool at 158 °C feeding two channels is shown in panel **(B)**. **(C)** Front of the sulfur flow with a delta-like morphology, reaching up to 108 cm wide and a temperature of 124°C. Panels **(D, E)** show the sampling procedure and measured temperatures of molten sulfur. White arrows point to the direction of the flow while red dots show the sampling site. Sample locations are presented in Figure 1C.

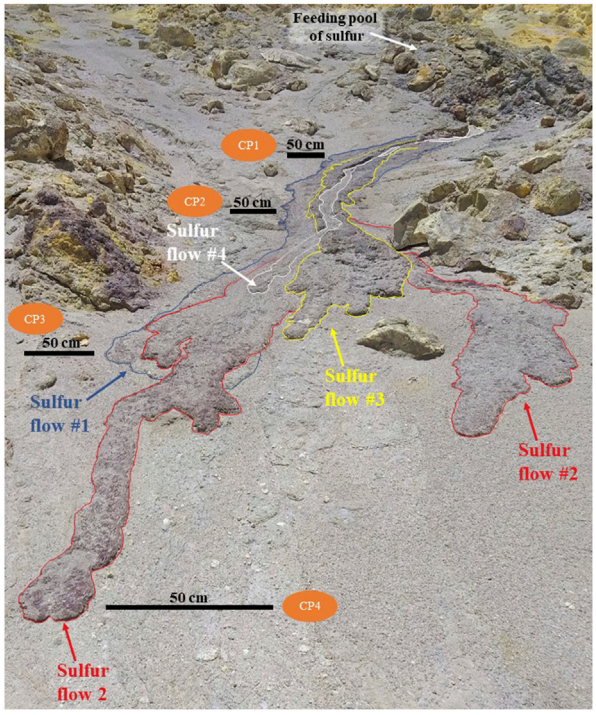

FIGURE 4
Sequence of the four sulfur flows identified during the April 2019 field excursion. They are sourced from the same sulfur pool observed in Figures 3A,D, and Supplementary Material S1. It is important to note that only sulfur flow #1 was observed live while flows #2, #3, and #4 occurred after fieldwork. Sulfur flows are marked in different colors according to their distribution and contact relationship. Four control points (CP) show scales of 50 cm according to the image perspective. The image is oriented to the south, then the flow #2 on the left and right branches correspond to the east and west flows in Table 1, respectively. The approximate total volume of the four sulfur flows is 0.89 m^3.

videos were recorded during fieldwork while the flows were still moving (Supplementary Material S1). Satellite images were acquired in stereo mode by Pleiades, a French satellite tasking Lastarria, in 2016 and in 2022 (Figures 2A–D). The satellite captures grey scale panchromatic images (PM) with a resolution of 0.5 m, which is sufficient to depict prominent changes in fumarolic field 1 (Figure 2). We processed the data using the satellite processing function in Agisoft Metashape 2.0, using the rational polynomial coefficient (RPC) information for georeferencing. To ensure the accurate stacking of the two datasets, we defined ground control points at 24 identified locations. Following the dense cloud generation of 24 million points, digital elevation models and orthomosaics were generated. For this study, we concentrated only on fumarolic field 1 and searched for changes by visually comparing the 2016 and 2022 datasets (Figure 2). The location, dimensions, and topography of the sulfur flow area are important constraints for the further analysis and contextualization of other observations.

Video files of one active and advancing sulfur flow (flow #1 of the 2019-flows, Figures 3, 4) were recorded using a mobile phone (Xiaomi Redmi Note 7; Supplementary Material S1). The videos were stabilized and time-stamped image files were extracted for geometric reconstruction and velocity estimation. The pixel-to-meter transformation was performed using the widths of the flows observed in the orthomosaic data. For the geometric reconstruction, we used 767 extracted images in the structure-from-motion workflow using Agisoft Metashape 2.0, defined GCPs from the field to constrain the dimension (width of the front of 108 cm), and calculated 110,000 tie points. From this, an orthomosaic with a 0.5 cm pixel size, and a digital elevation model with a resolution of 2 cm were created. These results were used to constrain the morphometry of flow #1. For velocity estimation, we imported the image database into DAVIS (Lavision Inc.), a particle image velocimetry (PIV) approach that aims to search for point and region transformations in fluid dynamics regimes.

3.2 Temperature measurements

Temperatures were measured using a K-type thermocouple thermometer from Hanna Instruments (HI935002) connected to a Hanna Instruments flexible probe (HI766Z) built-in stainless steel to measure temperatures of up to 1,100°C. Temperatures were measured at the sulfur pools and at the proximal and distal sections of the sulfur flow (Figure 3).

3.3 Sampling and analytical procedures

The sulfur flow was sampled twice; once during the active flow in January 2019 (Figure 3) and again 3 months later (April 2019) when the flow had cooled and allowed closer inspection (Figure 4). First, the samples were introduced into glass flasks (Figures 3D,E) and cooled at ambient temperature (Supplementary Material S1). Once solidified, the samples were stored in sealed plastic bags and sent to the laboratory for X-ray diffraction, scanning electron microscope, and trace element analysis. In April 2019, a physical description of the solidified sulfur flows was provided.

X-ray diffraction was performed using a Bruker D8 Advance diffractometer at Unidad de Equipamiento Científico (MAINI, Universidad Católica del Norte, Chile). Before analysis, a representative fragment of the sample (~20 g) was powdered with an agate mortar, sieved (<0.075 mm), and mounted in plastic holders. Analyses were done with an accelerating voltage of 40 kV and a current intensity of 30 mA, with Cu Ka radiation (I = 1.5406 Å) using a graphite monochromator and scintillation detector. Samples were diffracted at a 2θ angle of 3–70°, with steps of 0.020° and a 5 s integration time. Diffractograms were processed using the Bruker DIFRACT-SUITE software, which identifies and semi-quantitatively calculates the mineral phases and degree of crystallinity (amount of crystalline phases *versus* non-crystalline or amorphous phases).

Texture and quantitative microanalyses of the collected samples performed using a Hitachi TM-1000 environmental scanning electron microscope equipped with an energy dispersive spectrometer (ESEM-EDS) at the Laboratorio de Petrografía y Microtermometría of the Instituto de Geofísica UNAM. Selected samples and individual crystals were analyzed in detail using a field–emission scanning electron microscope (FE-SEM, Hitachi SU5000) to retrieve high-resolution images at the MAINI facilities. This device also included an Energy Dispersive X-Ray Spectrometer (EDS) for acquiring detailed chemical maps and accurate point analyses. Before the analysis, a representative fragment of the sample (<3 cm in size) was mounted on Al holders and coated with carbon. Samples were analyzed using an accelerating voltage of 20 kV and a 20–40 s integration time through the Hitachi SU5000 while an accelerating voltage of 15 kV and 37–43 s integration time were employed using the Hitachi TM-1000 equipment.

Trace element concentrations (As, Cd, Co., Cs, Cu, Li, Mo, Ni, Pb, Rb, Sb, Sn, Th, U, and Zn) were determined using high-resolution inductively coupled plasma mass spectrometry (HR-ICP-MS; Element 2XR Thermo Fisher Scientific). First, the samples were powdered and sieved (#270) at the Universidad Católica del Norte and then sent to the geochemistry laboratories of the Helmholtz Centre, Potsdam (GFZ, German Research Centre for Geosciences, Germany) for acid digestion and trace element analyses. The acid digestion procedure included the drying of powders (105°C); weighing into 15 mL Teflon vials (Savillex®); and decomposed using HF, HNO_3, and $HClO_4$ (ULTREX® II), following the protocol of Romer and Hahne (2010). Analytical results were supervised using internal (SCO-1; Romer and Hahne, 2010) and external (Imai et al., 1995) standards.

Stable sulfur isotope ratios were measured using a femtosecond laser ablation (fs-LA) system at GFZ Potsdam in combination with a multi collector ICP-MS (Thermo Fisher Scientific Neptune, equipped with a Neptune Plus Jet Interface) (Oelze et al., 2021). A laser beam (~25 μm in diameter) was continuously scanned over the sample surface (ablation area of 100 × 100 μm) for 100 s, with subsequent background measurement for 150 s. Samples were quantified using the standard sample bracketing (SSB) approach with IAEA-S1 as the primary reference material. Every measurement session contained a range of reference materials (e.g., MASS-1 and Balmat pyrite) that were repeatedly analyzed between sample measurements for comparison with published S isotope values. Raw isotope data processing and background corrections were performed after applying several data rejection and acceptance criteria (e.g., Oelze et al., 2021). The most imperative data rejection/acceptance criteria were as follows: i) only the $^{34/32}S$ and $^{33/32}S$ ratios were used for the calculation, which deviates by < 3 s (standard deviation) from the sample mean; ii) only results that follow the mass-dependent terrestrial fractionation line in a three-isotope-plot of $^{34/32}S$ vs. $^{33/32}S$ within analytical uncertainties; and iii) had a mass bias drift between the two bracketing calibrators of <0.30‰ were accepted and reported in this study. We reported the sulfur isotope values ($\delta^{34}S$) in delta notation as:

$$\delta^{34}S = \delta^{34/32}S_{VCDT} = \left[\left({}^{34}S/{}^{32}S\right)_{sample} / \left({}^{34}S/{}^{32}S\right)_{VCDT} \right] - 1 \quad (1)$$

4 Results

4.1 Morphometry and characteristics of the sulfur flow

Satellite images acquired in 2016 and 2022 showed two sulfur flows that emerged at approximate elevations of 5,100 and 5,114 m above sea level (m asl), referred to as the 2016–2022- and 2019–flows, respectively (Figure 1C, 2D). The exact dates of the 2016–2022-flows are unknown, but can be constrained between 2016 and 2022, most likely between our field visits in April 2019 and February 2020. The 2016–2022-flows comprise several partially overlapping flow units, up to 55-m-long and 5.3 m wide, and emerge from a 16-m-wide fumarole cluster (at 68.52189° W, 25.15458° S). They terminated at 5,074 m, thus descending with an average dip of 25°.

At 5,114 m asl, the 2019-flows were better identified in our field photos and videos taken in January and April 2019 (Figures 5A, B). Four flows can be identified (Figure 4), and flow #1 is well recorded, allowing us to construct a three-dimensional model and determine the geometric characteristics. Sulfur flow #1 (*cf.* Records in Supplementary Material S1) reached a 9.5 m distance from the source, a maximum width of 108 cm, and an average thickness of 3 cm (Figure 5). The three-dimensional model shows that the thickness was not uniform with a deposition zone at the lower front (up to 4 cm thick). Colored orthomosaics show a dark brownish central area, surrounded by pale-gray sulfur deposits (Figure 5C). The dimensions of the flow structure were well determined, although the source at the fumarole vent is not visible here because of poor image quality. The morphology at the middle distance shows defined flow channels, which are most visible in slope maps and topographic profiles (Figures 5D,E), and

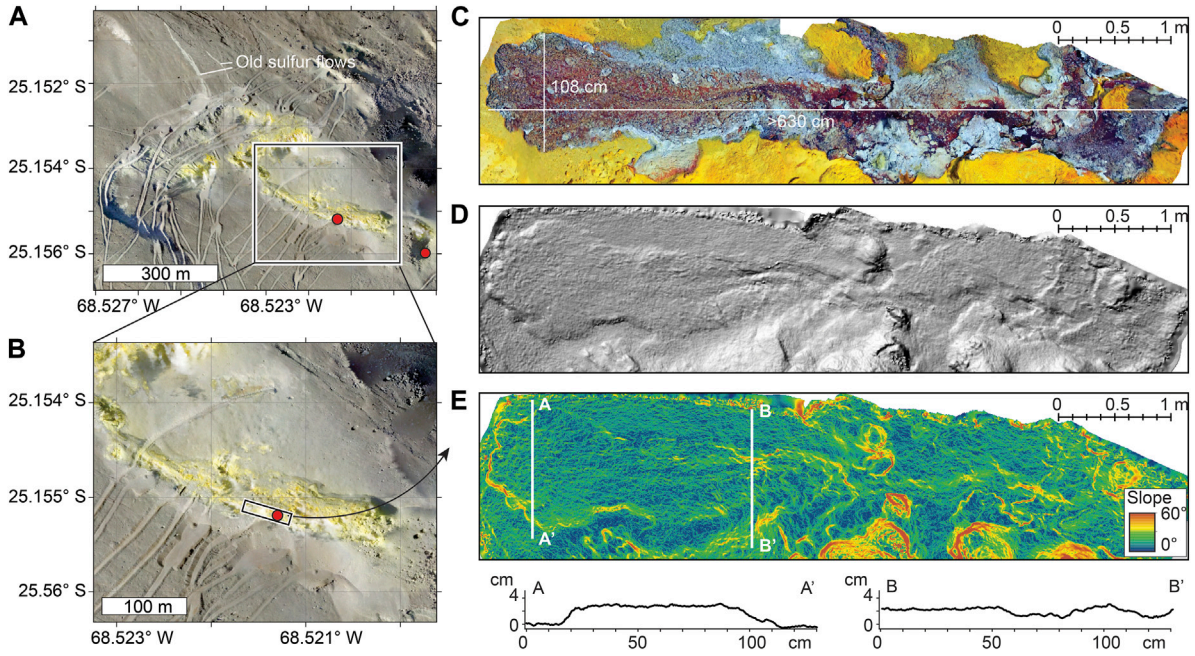

FIGURE 5
Drone and field morphometric analysis of the sulfur flow #1. **(A)** Orthomosaic of drone photographs showing locations of sampling sites, and **(B)** close-up of January 2019 flow location. North is up. **(C)** Mosaic of field photographs showing the extent and dimensions of the sulfur flow. North is to the upper left. **(D)** Shaded relief of sulfur flow shows the near-vent region (right) and accumulation zone (left), and erosion and dams in the middle section. **(E)** The slope map shows the steepest slopes in front. Topographic profiles A-A′ and B-B′ are provided below the slope map: the horizontal axis is the distance, and the vertical axis is the height difference (in cm).

shows minor deposition of material up to a thickness of approximately 1 cm and central erosion into the deposited materials (Figures 5D,E). The levees are up to 0.8 cm high, traceable over 180 cm, and oriented in the flow direction, representing traces of prominent shear zones during flow. The flow front fans out and thickens in the depositional zone with an irregularly shaped rope-like frontal thrust (Figures 3C, 5D).

Sulfur flow #2 presented two branches (east and west) reaching a distance of 12 and 9.8 m distance from the source, respectively, up to a width of 0.8 m and a maximum thickness of 5 cm. Sulfur flow #3 was shorter and thicker than the previous flows, being 7.8 m long, 7 cm thick, and up to 1 m wide near the front. Finally, sulfur flow #4 was the shortest and thinnest flow, 7 m in length, 1 cm in thickness, and up to 18 cm in width. Furthermore, contiguous areas (Supplementary Figure S2.2) show several sulfur flows sourced from the same site as the four flows shown in Figure 4. The sulfur flow (Supplementary Figure S2.2) exhibited poorly developed rope-like morphologies with an average thickness of only 2 cm. Field measurements of the #1, #2, #3, and #4 flows (Figure 4), and flows in the contiguous area (Supplementary Figure S2.2) are summarized in Table 1. Based on the maximum length, average thickness, and average width (Table 1), we concluded that the total volume of the 2019-flows was 1.45 ± 0.29 m^3. The most important source of uncertainty regarding this volume is the average thickness because we have limited point measurements that vary between 1 and 7 cm, ignoring thickness fluctuations along the flow. Therefore, a relative uncertainty of 20% was considered for volume computations.

Cross-sections of the solidified 2019-flows revealed a generally high vesicularity (visual estimation of 30%–50%; Supplementary Figure S2.3), although fewer vesicular areas occasionally appeared towards the base of the flow, close to the contact with the yellowish substrate (Supplementary Figure S2.3C). Furthermore, the incorporation of accessory fragments of lithics and sulfur crystals of minor sizes (less than 0.5 cm) is also depicted in Supplementary Figure S2.3 and field observations.

4.2 Video recording, particle velocimetry, and temperature recordings

The January 2019 video recordings showed the sulfur flow #1 in reddish-brown colors, with a continuous bubbling due to the constant gas input at the pool bottom, presenting a temperature of 158°C (Figure 3A). In the upper part, the sulfur pool overflow produced two molten sulfur channels moving downslope (11–15° on average, 24° maximum; Figure 3B) at an average speed of 0.069 m/s. Molten sulfur gradually slowed until it stopped because of the diminished terrain slope and partial solidification of the sulfur flow surface, as evidenced by the grayish crusts and rope-like textures (Figures 3, 5C; Supplementary Material S1). Subsequently, flow #1 showed a delta-type morphology and a measured temperature in the front of 124°C (Figure 3A, Figure 3C). Higher velocities were found at the center of the flows, where the margins showed large rotational shear components and the formation of small levees. As the surface is

TABLE 1 Physical parameters of the 2019-flows considering the four sulfur flows observed in Figure 4 and contiguous flows in Supplementary Figure S2.2. Physical parameters are reconstructed based on field measurements and photography analysis. The total volume of molten sulfur is 1.45 ± 0.29 m^3, considering a 20% uncertainty in the thickness measurements. CP: control points at different distances from the source in Figure 4. Bold values represent summarized parameters considering other volcanoes with evidence of molten sulfur manifestations.

Sulfur flow #	Max. Length (m)	Width (m)	Average thickness (m)	Volume (m^3)	Min. Time active (min)	Emission rate (m^3/h)	Speed (m/s)	Measured temperature
1	9.5	CP1: 0.70 CP2: 0.70 CP3: 1.08 CP4: N.A. aver.: 0.83	0.03	0.24	109	0.13	0.069	124–158 °C
2 (east)	12.0	CP1N.A. CP2N.A. CP3: 0.75 CP4: 0.20 aver.: 0.48	0.05	0.28	151	0.22	N.A.	N.A.
2 (west)	9.8	CP1N.A. CP2: 0.15 CP3: 0.80 CP4: N.A. aver: 0.48	0.03	0.14			N.A.	N.A.
3	7.8	CP1: 0.40 CP2: 0.40 CP3N.A. CP4: N.A. aver.: 0.40	0.07	0.22	81	0.16	N.A.	N.A.
4	7.0	CP1: 0.10 CP2: 0.18 CP3N.A. CP4: N.A. aver.: 0.14	0.01	0.01	67	0.009	N.A.	N.A.
Contiguous area (Fig. S2.2)	8.0	3.5	0.02	0.56	N.A.	N.A.	N.A.	N.A.
Summary Lastarria volcano	**< 12**	**0.1–0.8**	**0.01–0.07**	**1.45 ± 0.29**	**> 408**	**0.009–0.22**	**0.069**	**124–158 °C**
2019-flows								
Lastarria volcano	**350 and 200**	**1.0–2.5**	**0.1–0.2**	**> 500**	**30 and 50**	**64.8**	**0.12**	**N.A.**
Old flows[a]								
Azufre volcano (Ecuador)[b]	**225**	**< 30**	**< 0.5**	**1755**	**N.A.**	**N.A.**	**N.A.**	**N.A.**
Shiretoko-Iozan volcano (Japan)[c,d]	**1,400**	**N.A.**	**N.A.**	**1759–2000**	**Four days of intermittent sulfur emission**	**~20[e]**	**≥0.24[f]**	**Measured: 118 °C** **Estimated: 130–140 °C**
Turrialba volcano (Costa Rica)[g]	**175**	**10**	**N.A.**	**N.A.**	**N.A.**	**N.A.**	**0.0009[h]**	**90 °C**

(Continued on following page)

TABLE 1 (*Continued*) Physical parameters of the 2019-flows considering the four sulfur flows observed in Figure 4 and contiguous flows in Supplementary Figure S2.2. Physical parameters are reconstructed based on field measurements and photography analysis. The total volume of molten sulfur is 1.45 ± 0.29 m^3, considering a 20% uncertainty in the thickness measurements. CP: control points at different distances from the source in Figure 4. Bold values represent summarized parameters considering other volcanoes with evidence of molten sulfur manifestations.

Sulfur flow #	Max. Length (m)	Width (m)	Average thickness (m)	Volume (m^3)	Min. Time active (min)	Emission rate (m^3/h)	Speed (m/s)	Measured temperature
Poás	**83**	**N.A.**	**N.A.**	**12.5**	**N.A.**	**N.A.**	**N.A.**	**Estimated: 113–160°C**

[a]Naranjo (1985; 1988).
[b]Colony and Nordly (1973).
[c]Yamamoto et al. (2017).
[d]Imai et al. (1995) and references therein.
[g]González et al. (2015).
[h]Personal communication by an anonymous reviewer.
Mora-Amador et al. (2019).
[e]Calculated by dividing the total volume over 4 days of activity.
[f]Calculated dividing the maximum distance of 1,400 m across 4 days of activity. This value must be considered as the minimum because sulfur flows at Shiretoko-Iozan consisted of intermittent and overlapped flows of molten sulfur.
N.A.: not applicable/measured.

TABLE 2 Chemical concentration of trace elements (ppm) in flows and pools of molten sulfur collected in January 2019. Average concentrations of host rocks (lavas and pyroclastic flows) used in enrichment factor computations were extracted from Naranjo (1992, 2010), Trumbull et al. (1999), and Robidoux et al. (2020).

Sample	F1A	F1B	F2	Average References host rocks
	Sulfur pool	Sulfur pool	Sulfur flow	
Li	0.3	0.2	0.6	25
Sc	0.1	0.1	0.2	12.7
V	1.4	1.1	2.5	142
Co.	0.2	0.2	0.6	17
Ni	0.7	0.7	1.1	32
Cu	12	11	18	38
Zn	18	12	4.3	74
Ga	0.2	0.2	0.4	19.7
As	40,907	42,268	6,979	2.3
Rb	3.0	2.1	5.6	127
Sr	5.3	3.6	7.9	514
Zr	5.1	5.2	11	190
Nb	0.7	0.6	1.1	11.3
Mo	0.6	0.5	2.1	4.2
Cd	0.03	0.05	0.54	0.19
Sn	3.4	2.9	1.2	2.0
Sb	6.8	5.9	56	1.53
Cs	0.3	0.2	0.6	7.9
Pb	4.9	4.6	31	16
Bi	20	18	10	0.4
Th	0.6	0.4	1.4	25
U	0.2	0.2	0.5	6.35

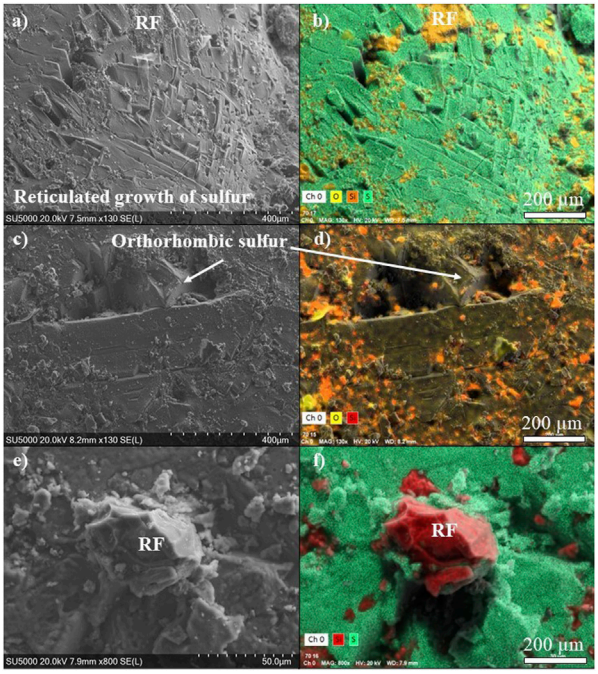

FIGURE 6
BSE-images (left panels) and EDS-chemical maps (right panels) of the sulfur flow sample (F2) showing their textural and morphological characteristics. These images show the reticulated growth of sulfur **(a–d)** with significant amounts of rock fragments (RF) in red to orange colors **(e, f)**.

blocky and uneven, steep slopes represent higher velocities, locally reaching even 0.4 m/s. In contrast, the low–slope sections were related to lower velocities and the formation of sulfur puddles of up to 108 cm wide (Figure 3C). We note that, similar to sulfur pools, the sulfur flows showed intense bubbling as they moved downslope, especially in areas with fewer slopes where flows stagnated (Supplementary Material S1).

4.3 Chemistry and mineralogy

The total trace element concentrations in sulfur flow #1 (Figure 4) ranged from a few ppm to 42,268 ppm (Table 2). Arsenic reached the highest concentrations, especially in sulfur pools, with values up to five orders of magnitude higher than those of the other analyzed chemical elements. Lead, Bi, Cu, Zn, Rb, Sr, Zr, Sb, and Sn presented average concentrations between 1 and 56 ppm. In contrast, Li, Cd, Th, U, Co., Sc, Ni, Ga, Nb, and Ga had average concentrations of less than 1 ppm.

X-ray powder diffraction analysis of the sulfur pool (F1A, F1B) and sulfur flow (F2) samples showed the presence of orthorhombic native sulfur (Supplementary Material S3) with crystallinity degrees of 45% and 64% in the sulfur pool and sulfur flow samples, respectively. A more detailed inspection using high-resolution BSE (back-scattered electrons) imaging allowed us to identify the microtextures of the samples and the size/shape of the accessory fragments. SEM-EDS analysis detected Al, As, Fe, K, O, S, Si, Ti, I, and Pb, with S being the most abundant and displaying reticular and arborescent textures (Figure 6A–F). Additionally, distinctive crystalline phases <100 µm in size containing As, I, and Pb were observed. The As-bearing phases were identified as possible orpiments with iodine impurities, realgar, and arsenolite, whereas the Pb-bearing minerals were linked to galena (Figures 7C,D, Supplementary Material S4). Fragments containing Si and O, plus minor Fe, K, Al, and Ti of 20–200 µm in size, were ascribed to rock fragments (RF in Figure 6) incorporated during the movement of the sulfur flow over the substrate. Conversely, the presence of As, I, and Pb (Figure 7) can be ascribed to magmatic degassing.

4.4 Sulfur isotopic composition

The sulfur isotopic composition in the F2 sample was -6.10‰ vs. VCDT. This value is the first result for $\delta^{34}S$ reported for Lastarria volcano; it is fairly light compared to average MORB glasses (–0.91‰ ± 0.50‰; Fischer et al., 1998). The obtained value of –6.10‰ is heavier than the range observed for elemental sulfur at Poás (–12.3 to –9.4‰; Oppenheimer, 1992; Rowe, 1994) and within the range (–9 to +7‰; Ueda et al., 1979) obtained for 44 different volcanic sites in Japan. Then, our $\delta^{34}S$ value is closer to the lighter values found in floating spherules at Kawah Ijen (–4.2 to –1.4‰; Delmelle et al., 2000; Kusakabe et al., 2000) and subsurface native sulfur at Campi Flegrei (–5.5‰ to 0‰; Piochi et al., 2015). Conversely, isotope values at Lastarria contrast with those of 0 to +10‰ found at Nea Kameni Islet in Santorini (Greece; Hubberten et al., 1975).

5 Discussion

5.1 Temperature and viscosity relationship

Field observations and measurements allowed for better understanding of the physicochemical conditions controlling the emplacement mechanisms of molten sulfur. Measured temperatures of 124°C in sulfur flows and 140 and 158°C in sulfur pools (Figure 3) represent one of the few records of temperatures from these types of manifestations, which are higher than those reported by Ikehata et al. (2019) of 124.7°C in a yellow-amber molten sulfur pool at Hakone volcano. The temperature of molten sulfur has a direct relationship with viscosity. For example, pure sulfur melts at 119°C, and its viscosity decreases until 159°C, increasing rapidly by four orders of magnitude at approximately 160°C because of the polymerization of sulfur molecules (MacKnight and Tobolsky, 1965; Greeley et al., 1990; Oppenheimer, 1992). Although viscosity measurements were not available in this study, there were evident differences in this physical parameter between the flows and pools of sulfur, which could be associated with the *in situ* measured temperatures (Figure 3). For example, the sulfur pools showed variable viscosities, with those located in the upper part of fumarolic field 1 being more viscous than those feeding sulfur flow #1 (Figure 3A). This difference can be explained according to variable measured temperatures (140 vs. 158°C) and then the stronger influence of high-temperature gases feeding the bubbling

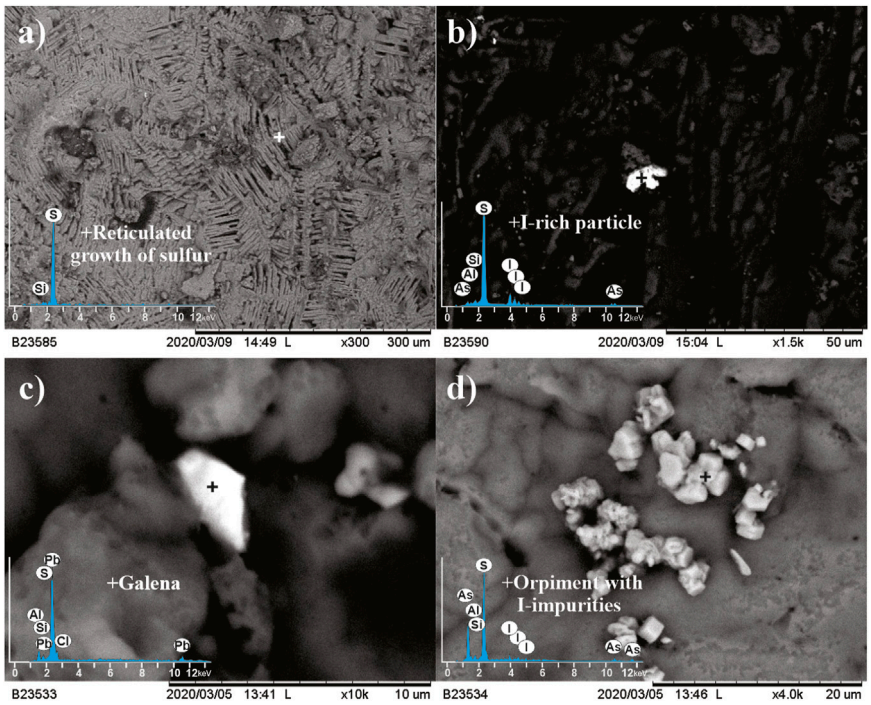

FIGURE 7
BSE-image showing the distribution of chemical elements and minerals phases on solidified molten sulfur samples. **(A)** BSE-image showing the reticulated growth of sulfur. **(B)** Iodine rich particle. **(C)** galena particle. **(D)** presence of orpiment with iodine impurities. EDS spectrums are presented in Supplementary Material S4.

and less viscous sulfur pool at 158°C. In contrast, sulfur flow #1 showed an intermediate viscosity compared to the two sulfur pools (Figure 3, Supplementary Material S1) and lower recorded temperatures (124°C), increasing its viscosity gradually with distance from the source and decreasing slope. In general, sulfur flows observed in Lastarria had similar bubbling processes and colors to the sulfur pool in the 15-2A fumarole at the Hakone volcano (e.g., Ikehata et al., 2019).

One of the most important features of molten sulfur observed at the Lastarria volcano in January 2019 was its dark brownish to reddish color. When molten sulfur occurs, the color is directly related to the temperature and viscosity (Takano et al., 1994). For example, according to the simple temperature-viscosity-color correlation, the dark-brownish color of our samples could suggest sulfur temperatures of ~200°C and very high viscosities. However, our measured temperatures are within a narrow range of 124–158°C, and the sulfur flows seemed to be low viscous. Therefore, impurities within the molten sulfur can explain the dark brownish color and lower measured sulfur temperatures (Kargel et al., 1999). For instance, shades of red, brown, and orange in fumarolic deposits at the Lastarria volcano correlate well with As enrichment and As-bearing minerals (Inostroza et al., 2020). Therefore, high As contents (Table 2) and As-bearing minerals found in molten sulfur (Figure 7 and Supplementary Material S4) suggest that the brownish to reddish shades in the 2019-flows were more likely due to As impurities instead of an increased molten sulfur temperature. A similar conclusion was obtained by Kargel et al. (1999), who revealed substantial viscosity changes in sulfur when it contained impurities of As and other elements such as Cl and I. Consequently, impurities of As must be considered when studying the natural occurrence of reddish-to-orange molten sulfur manifestations (e.g., Greeley et al., 1990; Kargel et al., 1999).

5.2 Trace element enrichment

The 2019-flows had significant concentrations of trace elements, with extremely high concentrations of As. The enrichment factor (EF) is one of the most important parameters to describe the enrichment of trace elements in a geochemical medium relative to a reference material (EF; Zoller et al., 1974). For the Lastarria volcano, the EF values for a given element from the sulfur pools and sulfur flow were compared with volcanic pristine host rocks according to the following expression:

$$EF = (X/Y)_{sample} / (X/Y)_{host-rocks}, \quad (2)$$

where "X" is the chemical concentration of a given element in the sample (i.e., molten sulfur) and host rocks while "Y" is the concentration of a reference chemical element in both the sample and host rocks. In this case, the reference element "Y" should be a refractory and non-volatile element with low concentrations in the sample and host rocks to enhance the EF values. Previous studies have selected Ti (Symonds et al., 1987), Al (Zoller et al., 1983; Varrica et al., 2000), Mg (Aguilera et al., 2016), Be (Moune et al., 2010), Th (Calabrese et al., 2011), or Sc (Olmez et al., 1986) as a chemical element of reference. In this case, Ti, Al, and Mg were not

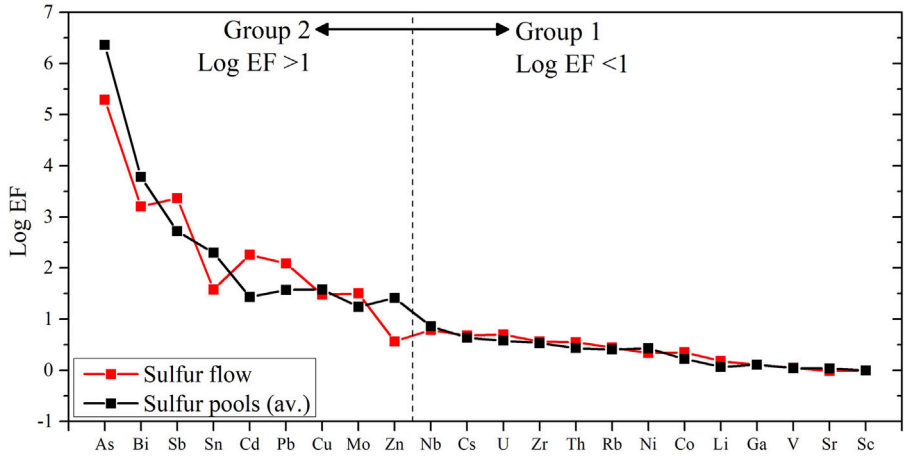

FIGURE 8
Sc-based Enrichment Factors (EF) of the 2019-flows, including two pools (black squares) and one flow (red squares) of molten sulfur. The sulfur pool line represents the average value from F1A and F1B (Figure 3; Table 2).

in our database (Table 2), whereas Th appeared to be slightly enriched compared to Sc, particularly in the sulfur flow sample. Therefore, Sc was selected as the reference element. The rock reference database was constructed from the average concentrations of lava and pyroclastic rocks from the Lastarria volcano (Table 2; Naranjo, 1992, Naranjo, 2010; Trumbull et al., 1999; Robidoux et al., 2020).

The Log EF values for the 22 trace elements varied between ~0 and 6.4. The elements were divided into two groups (Figure 8). Group 1 includes those chemical elements with Log EF < 1 (Nb, Cs, U, Zr, Th, Rb, Ni, Co., Li, Ga, V, Sr, and Sc), characterized by volatilities close to zero at temperatures <400°C and, in general terms, affinity with silicate melts instead of S-rich fumarolic fluids. Similar $(X/Y)_{sample}$ and $(X/Y)_{host\text{-}rocks}$ ratios (Eq. 2) suggest that these elements were incorporated into the flow as rock particles, likely because of erosive processes in the fumarolic conduit or erosion of the substrate surface as the flow moved downslope. Given the vigorous fumarolic activity, these processes are highly plausible for this volcano. Accidental fragments were observed in the SEM-EDS images (Figure 6) and cross-sections (Supplementary Figure S2.3), which agrees with the opalized basalt fragments in sulfur flows at the Azufre volcano (Galapagos; Colony and Nordlie, 1973) and rock fragments in old sulfur flows at Lastarria (Naranjo, 1988).

Group 2 corresponds to trace elements with Log EF > 1 (As, Bi, Sb, Sn, Cd, Pb, Cu, Mo, and Zn), mainly dominated by chalcophiles; they have a strong affinity with sulfur. The high EF of Group 2 elements indicates the influence of a deep and/or shallow magma chamber beneath the volcano, i.e., feeding chalcophile elements, and that these elements show volatile behavior in fumarolic emissions at the Lastarria volcano. Among these elements, As stands out, with EF values six orders of magnitude higher than those found in the host rocks. Such enrichments agree with the As-bearing minerals found in the SEM-EDS images (Figure 7; Supplementary Material S4), in addition to the As-enrichments and As-bearing minerals found in reddish fumarolic deposits at the Lastarria volcano (Aguilera et al., 2016; Inostroza et al., 2020). Similarly, Sb and Bi also showed a very high EF, even though no mineral phases containing these elements were found in the Lastarria volcano. In addition to the trace elements mentioned above, such as Sn, Cd, and Pb, chalcophile elements that are usually enriched in subduction-related fumarolic gases (Edmonds et al., 2018) also showed a high EF. We highlight iodine, which was detected forming mineral phases through SEM-EDS analyses (Figure 7), suggesting that it is present in high concentrations in fumarolic deposits and gases. This agrees with the chemical analyses reported by Aguilera et al. (2016), where it appears as the most enriched trace element in condensed gases. Aguilera et al. (2016) found similar EF patterns in fumarolic deposit samples and volcanic gas condensates, demonstrating that Lastarria samples were enriched in Sb, As, Cd, Se, Ni, Pb, and Cu. Such a good correlation between the chemical composition of molten sulfur and fumarolic deposits suggests that the molten sulfur observed in January 2019 corresponds to the melting of previously existing fumarolic deposits and/or that all of these species were transported by the same gas phase (e.g., Symonds et al., 1992; Taran et al., 1995).

Arsenic, Se, Sb, and Cu have been found at high concentrations in molten sulfur, either in subaerial sulfur flows or at the bottom of acid crater lakes (e.g., Stoiber and Rose, 1974; Oppenheimer and Stevenson, 1989; Kargel et al., 1999; Xu et al., 2000; Daga et al., 2017). Moreover, Hg, Mo, Au, Co., and Fe are also present in significant concentrations in floating S-rich spherules in the Poás and Copahue crater lakes (Xu et al., 2000; Daga et al., 2017). Molten sulfur found at the Lastarria volcano contains significant amounts of chalcophile trace elements, in agreement with similar manifestations worldwide, such as Poás or Copahue (Oppenheimer and Stevenson, 1989; Daga et al., 2017). The high EF of chalcophiles in subaerial and subaqueous molten sulfur can be ascribed to their selective scavenging during sulfur formation, which is favored by their chemical affinity and continuous supply from the gas phase (Symonds et al., 1992). Furthermore, chalcophile scavenging by sulfur was identified in sulfur precipitates during the sampling of condensed gases (e.g., Fischer et al., 1998). Unfortunately, there is a lack of quantitative trace element analyses in molten sulfur samples,

which hampers detailed comparisons between different volcanic systems.

As listed in Table 2, the As concentrations in the sulfur pools were six times higher than the same concentration in the sulfur flow, despite the fact that they were connected at a very short distance (<12 m between the sulfur pool and sulfur flow #1; Figure 3). This difference appears intriguing given the similar molten sulfur temperatures and colors of the pool and flow (Figure 3). The As-bearing crystalline and amorphous phases condense and precipitate or sublimate at temperatures lower than 300 °C (Mambo and Yoshida, 1993; Mandon et al., 2020), thus they can be efficiently trapped in S-rich melts. Consequently, the higher As concentration in the sulfur pools can be related to the condensation of the gas phase, whereas the lower concentration in the sulfur flow could be ascribed to As partitioning into the gas phase favored by continuous sulfur flow bubbling. This process should decrease the As concentration towards the flow front.

5.3 Volume and timing

Considering the four sulfur flows shown in Figure 4 and the contiguous area with molten sulfur (Supplementary Figure S2.2), the total volume of molten sulfur approaches 1.45 ± 0.29 m^3. This volume can be regarded as a modest value compared with the sulfur flows previously reported at the Lastarria, Azufre, Shiretoko-Iozan, and Poás volcanoes (Table 1). The volume estimated for the 2019-flows could increase considering the 2016–2022-flows (Figures 1, 2), which occurred during the same period; therefore, the accumulated sulfur volume may be significantly higher, although we do not consider that it could reach the volume of old flows at Lastarria. Pure sulfur was characterized by a density of 2.07 g/cm^3. However, the number of vesicles and accessory lithics decrease and increase this value, respectively. The approximate density of sulfur flows can be obtained using the percentages of sulfur, rock particles, and vesicles, as shown in Figure 6 and Supplementary Figure S2.3. Considering 50, 15, and 35% of sulfur, rock particles, and vesicles, respectively, a density of 1.43 g/cm^3 was calculated, which implies a mass of molten sulfur of 2.07 ± 0.41 tons for the 2019-flows.

Although several volcanoes are known for the presence of flows or pools of sulfur, the emplacement and speed of molten sulfur have only been observed in a few of them (e.g., Shiretoko-Iozan; Watanabe and Shimotomai, 1937; Watanabe, 1940). Video records at Lastarria volcano (Supplementary Material S1) indicate that the sulfur flow #1 (Figures 3, 4) was emplaced at an average speed of 0.069 m/s over a slope of 11–15°. However, the speed decreased to ~0.001 m/s when the flow reached flatter areas (<10°). These speeds are lower than those of 0.12 m/s estimated by Naranjo (1988) and also lower than those of 0.1–1.05 m/s reported in the case of pure molten sulfur (99.6% of purity) produced through the Harsh method (industrial sulfur flows produced by the injection of superheated water into wells drilled in sulfur-rich sediments; further details in Greeley et al., 1990). For the 2019-flows, field measurements and sampling took approximately 120 min to complete while sulfur flow #1 moved slowly downslope by approximately 2 m, indicating an average speed of 0.00028 m/s. Independent of these subtle speed variations, forward speeds at the sulfur flow front decreased notably because of the solidification of sulfur at temperatures close to 119°C (Figure 3C), producing layer stacking of semi-molten sulfur, forming lobes, and rope-like textures (Supplementary Video S1; Figure 5).

The computed speeds for the 2019-flows are clearly lower than those previously calculated/reported for other volcanoes (e.g., Shiretoko-Iozan, Lastarria, and Azufre volcanoes), suggesting that the time at which the longest sulfur flows occurred in these volcanoes may be notably underestimated. Accordingly, information on these times is limited. Indeed, recorded times have been estimated to be in the range of 30 min to 4 h depending on the volume of the sulfur melt, or by up to 5 days of discontinuous emission of molten sulfur, which occurred at Shiretoko-Iozan (e.g., Watanabe and Shimotomai, 1937; Watanabe, 1940; Naranjo, 1988).

By assuming that the high-speed zone (i.e., slope of approximately 20°) is located within the first 3 m from the source and maximum speeds were only reached in this area, whereas the low-speed zone was located at distances greater than 3 m, we can obtain an approximation of the time it took for the four flows presented in Figure 4 to reach the site where they were found in April 2019. For the first 3 m, the high-temperature and poorly viscous sulfur flowed down in only 44 s and then entered the low-speed zone until stopping. Within this flatter zone, sulfur flow #1 remained in motion for at least 108 min, sulfur flow #2 for 150 and 113 min (east and west branches, respectively), sulfur flow #3 for 80 min, and sulfur flow #4 for 67 min (Table 1). These computations suggest that the molten sulfur flows were active for at least 408 min (6.8 h), assuming that each flow occurred immediately, one after the other, without pauses. Using computed volume and "displacement times" of the molten sulfur, emission rates result in a range of 0.13–0.22 m^3/h for flows #1, #2, and #3 while flow #4 showed a speed of only 0.009 m^3/h (Table 1). Such emission rates differ notably from the 64.8 m^3/h estimated for the old flows at Lastarria (Naranjo, 1988) and ~20 m^3/h established for the Shiretoko-Iozan flow (Table 1; Yamamoto et al., 2017).

In general terms, the active sulfur flows observed at the Lastarria volcano appear to have different rheological properties from those reported for other volcanoes because they have moved slower and for a more extended time range. Then, the 2019-flows appeared in a very specific area with a limited total volume, suggesting the occurrence of local processes, such as fracture opening, instead of general heating of the fumarolic field. However, records of unavailable temperature variations could have helped constrain these hypotheses. Therefore, possible changes in the fumarole temperature cannot be completely ruled out.

5.4 Insights into the origin of molten sulfur

Elemental sulfur can be formed via several pathways. For instance, at relatively low temperatures (<350°C), native sulfur condenses in the presence of SO_2 and H_2S according to the following reaction 3) (Mizutani and Sugiura, 1966; Giggenbach, 1987):

$$SO_2\ (g) + 2H_2S\ (g) = 3S^0\ (l/s) + 2H_2O\ (g). \quad (3)$$

TABLE 3 Chemical composition (mmol/mol), location (UTM-WGS-84), altitude (meters above sea level; m a.s.l.), and measured temperature (°C) of gas samples collected in the vicinity of molten sulfur manifestations in January 2019. Data in Table 3 from Layana et al. (2023).

Sample	LT57	LT58	LT59
	Flow	Flow	Pool
Cord S)	25.1552	25.1552	25.1558
Cord W)	68.5212	68.5212	68.5195
T (°C)	268	360	290
H_2O	703	699	682
CO_2	175	186	188
HCl	4.6	5.2	4.9
HF	0.69	0.88	0.79
SO_2	33	41	39
H_2S	5.6	3.2	4.9
N_2	9.6	9.1	8.8
CH_4	0.00013	0.00011	0.00012
Ar	0.056	0.061	0.079
O_2	0.016	0.0085	0.0091
H_2	68	55	71
He	0.0011	0.0015	0.0009
CO	0.0087	0.0079	0.0096

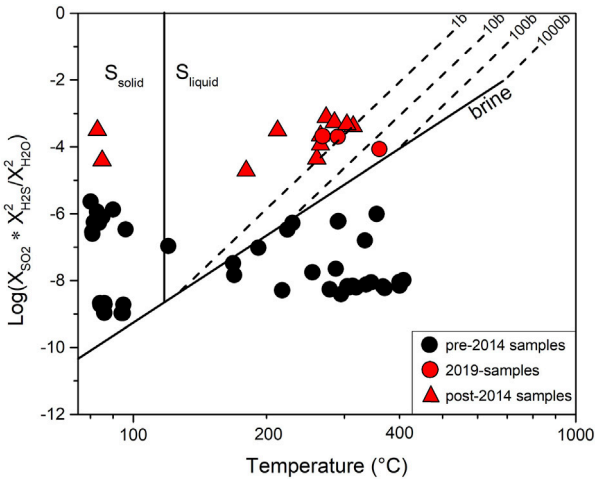

FIGURE 9
Saturation of Lastarria volcano fumarolic gases concerning native sulfur deposition (reaction 3). The plot includes sixty-three data collected between 2006 and November 2019 and published by Aguilera et al. (2012) and Layana et al. (2023). Modified from Giggenbach (1987).

Under similar temperature conditions, solid/liquid native sulfur can also be produced by SO_2 disproportionation in the presence of H_2O according to reactions 4) or 5) (Oppenheimer, 1992):

$$3SO_2\ (g) + 2H_2O\ (g/l) = 2H_2SO_4\ (aq) + 1/x\ S_x\ (l/s)\ \text{and} \quad (4)$$

$$4SO_2\ (g) + 4H_2O\ (g/l) = 3H_2SO_4\ (aq) + H_2S\ (g). \quad (5)$$

Reaction 3) has been primarily used to explain the formation of S-rich subaerial fumarolic deposits, whereas reactions (4–5) describe the formation of molten sulfur in subaquatic environments or volcanoes with well-developed hydrothermal systems (Oppenheimer, 1992). Furthermore, reactions (3–5) produce sulfur enriched in ^{32}S and then with $\delta^{34}S$ values <0 (Oana and Ishikawa, 1966; Ohmoto and Lasaga, 1982; Delmelle and Bernard, 2015), with the SO_2 disproportionation process (Reactions 4–5) producing native sulfur with strongly negative $\delta^{34}S$ values (as light as −12.3‰). However, for Lastarria volcano, the least negative $\delta^{34}S$ value ($\delta^{34}S$ = −6.10‰) differed from more negative values at Poás volcano. Additionally, reactions (4–5) require significant amounts of water inside the volcanic edifice (Delmelle and Bernard, 2015), contrary to what is thought for the Lastarria volcano, where the amount of water seems to be very limited (Aguilera et al., 2012). Therefore, reaction 3) can be postulated as an appropriate candidate for explaining the formation of molten sulfur, whereas SO_2 disproportionation (reactions 4 and 5) is an implausible process during the 2019-flows.

Inspection of historical data on fumarolic gases discharged at the Lastarria volcano (Aguilera et al., 2012; Layana et al., 2023) permits a better understanding of the physicochemical processes behind the 2019-flows and the feasibility of reaction 3) to form solid/liquid sulfur. Gas species involved in reaction 3) had the following behavior in 2006 and 2022 (excluding 2019 samples; all concentrations expressed in mmol/mol): SO_2 = 5.9 ± 0.9; H_2S = 2.5 ± 0.4; H_2O = 876 ± 4.6; SO_2/H_2S = ~2.3 (Layana et al., 2023). However, fumarolic gases collected during the 2019-flows contained the following concentrations: SO_2 = 38 ± 2; H_2S = 4.6 ± 0.6; H_2O = 695 ± 5.2; SO_2/H_2S = ~8.4 (Table 3). Notably, the samples collected in January 2019 (Table 3) showed the highest SO_2 and lowest H_2O concentrations ever recorded at the Lastarria volcano while the H_2S concentration almost doubled. The very high SO_2 compared to H_2S concentrations can be explained by the consumption of 2 mol of H_2S for every mole of SO_2 in reaction 3), depleting volcanic gases in H_2S and increasing the SO_2/H_2S ratios from an average of ~2.3, according to historical data, to ~8.4 in the 2019 samples (Table 3).

Following reaction 3) from Giggenbach (1987), solid/liquid sulfur formation is favored when fumarolic gases contain high concentrations of sulfur compounds and lower steam concentrations. Using the historical fumarolic gas dataset from Layana et al. (2023), detailed information was obtained by plotting the equilibrium constant for the deposition of elemental sulfur (Reaction 3) and the outlet gas temperatures (Figure 9). From this plot, the correspondence between the chemistry of fumarolic gases and molten sulfur observed in 2019 can be depicted, given that the gas samples fell into the liquid sulfur field. Remarkably, all of the >120°C gas samples collected after 2014 are similar to the 2019-samples in terms of the chemical composition (Figure 9), suggesting that the deposition of sulfur (liquid) could be favored by the chemistry of the fumarolic gases since this date. Simultaneously, Reaction 3) should produce significant amounts of H_2O, which

contradicts the low H_2O concentrations in the 2019 samples. This contrasting evidence could be ascribed to subsurface steam condensation or that the 2019-samples were collected in the presence of a depleted hydrothermal system, a process induced by an increase in degassing from a shallow magma chamber (Lopez et al., 2018; Layana et al., 2023).

The question that arises is why liquid sulfur was not frequently observed during the sampling procedures after 2014. Only the January 2019 flows were active, besides another 55-m-long sulfur flow that was active sometime between 2016 and 2022 (Figure 2D). Occasional visits to this volcano (only a few days every year) owing to access difficulties reduce the possibility of observing this phenomenon. Despite favorable physicochemical conditions for native sulfur formation, we believe that molten sulfur manifestations are sporadic events triggered by mechanical effects, such as the opening of new fractures or changes in host rock permeability (e.g., Rouwet et al., 2017). This sporadicity also explains the occurrence of molten sulfur only in specific sections of the fumarolic field, weakening the theory that sulfur flows are produced by the general melting of previously formed sulfur crusts owing to the heating of the fumarolic field. However, partial melting of sulfur crusts was recorded on the walls of the 158 °C sulfur pool (Supplementary Material S1; Figure 3A), implying that favorable physicochemical conditions for fumarolic gases and then partial melting of fumarolic deposits are behind the formation of pools and flows of molten sulfur.

Volcanoes such as Poás, Turrialba, and Copahue (González et al., 2015; Daga et al., 2017; Salvage et al., 2018) have shown molten sulfur before or during eruptive periods, especially during phreatic activity, prompting researchers to link these phenomena and even suggesting the occurrence of molten sulfur as a precursor of volcanic activity. For the Lastarria volcano, there are no historical records of eruptive activity. However, ongoing ground deformation in the Lazufre area (uplift of up to ~3 cm per year) and significant changes in the chemistry of fumarolic gases place this volcano in continuous unrest, which has been attributed to a pressurized magma chamber located at depths of 7–15 km; changes in the chemistry of fumarolic gases could be explained by a sequence of events that produced the acidification and depletion of the hydrothermal system, allowing the passage of less scrubbed magmatic fluids (Layana et al., 2023). Coincidentally, the 2019-flows occurred during a period that seemed to have started in 2014, when the volcano reached its peak activity, emitting high concentrations of SO_2, H_2S, HCl, and HF (Layana et al., 2023). The ongoing unrest satisfies the physicochemical conditions necessary for the formation of molten sulfur, and the occurrence of new sulfur flows cannot be ruled out. Consequently, molten sulfur witnessed at Lastarria volcano seems to be more related to ongoing unrest than to precursory eruptive activity, so it cannot be directly linked with eruptive activity.

6 Conclusion

Physical and chemical characterizations of pools and flows of molten sulfur observed in January 2019 at the Lastarria volcano were reported and compared with known cases such as Shiretoko-Iozan, Azufre, or old Lastarria flows. The sulfur flow was active for ~7 h, moving downslope slowly (~0.0069 m/s) even when it appeared less viscous. A total volume of 1.45 ± 0.29 m^3 of molten sulfur is estimated during the 2019 flows, a modest volume compared to the Shiretoko-Iozan, Azufre, and old Lastarria flows. At the same time, the Lastarria sulfur flows appear to have been active for a longer time than the old Lastarria flows. These rheological features suggest that the 2019-flows behaved slightly differently than expected. The information collected in this study is significant for understanding this phenomenon in future studies. Moreover, it can be presumed that the old Lastarria flows (up to 350 m in length) remained active for a longer time, significantly exceeding previous reports of 50 min.

Molten sulfur manifestations stand out because of their reddish to brown shades, variable temperatures between 124 and 158°C, and a visible viscosity that increases as they move away from the source. Mineral analysis of the solidified sulfur showed that orthorhombic native sulfur was the dominant mineral phase, which also contained As-bearing minerals, galena, and accessory Si-rich rock fragments. Arsenic was the most abundant trace element in the molten sulfur samples, followed by Bi, Sb, Sn, and Cd. In agreement with previous studies, As seems responsible for the reddish colors, suggesting that the color of molten sulfur could be more influenced by chemical impurities than higher temperatures.

The origin of molten sulfur at the Lastarria volcano can be attributed to enhanced sulfur condensation due to fumarolic gases enriched in SO_2 and H_2S, likely combined with changes in the permeability of fumarolic conduits. This explains why molten sulfur was observed only in a specific area of the fumarolic field. The sequence of events can be summarized as follows: i) fracture opening allowed the passage of S-rich gases, ii) sulfur condensed and partially melted the surrounding rocks at the vent, iii) continuous sulfur condensation produced a sulfur pool overflow, forming sulfur flows, and iv) finally, quenching of sulfur flows occurred because the flow temperature decreased. When sulfur moves downslope, it degasses, producing an As partition into the gas phase. Although the origin of molten sulfur is relatively well constrained, questions remain about which physicochemical processes in the magmatic-hydrothermal system trigger permeability changes. Given that molten sulfur was noticed in a specific area of the fumarolic field, we suggest that the general heating of the fumarolic field would not fully explain the 2019-flows. Therefore, such a common theory applied to other volcanoes could be questionable at the Lastarria volcano.

The generation of molten sulfur is a particular phenomenon that requires the attention of the scientific community, especially in volcanoes where this phenomenon occurs sporadically, as it may be related to possible eruptive activity or disturbances that may occur within the magmatic-hydrothermal system, as in the case of Lastarria. Further studies must be conducted to better understand the physicochemical processes underlying this phenomenon and their relationship with volcanic unrest. New events, such as those observed in January 2019 in Lastarria, will guide future research.

Data availability statement

The original contributions presented in the study are included in the article/Supplementary Material, further inquiries can be directed to the corresponding author.

Author contributions

MI, BF, FA, SL, and TW contributed to study conception, design, and writing. MI, FA, and MZ: Collected samples. BF wrote the first draft of the manuscript and organized the database. MI, FA, SL, TW, and MZ revised and corrected of the manuscript. MI, AR, and MO performed mineral and chemical analyses. All authors contributed to the article and approved the submitted version.

Funding

MI was funded by ANID-PCHA/Doctorado Nacional/201621160172. SL was funded by ANID-PCHA/Doctorado Nacional/21160276. This study was partially funded by FIC-R BIP 30488832-0 project "Mitigación de los Riesgos Asociados a Procesos Volcánicos en la Región de Antofagasta", National Research Funding Competition FONDECYT Regular 2021 Code 1211220, and by the internal project of the Instituto de Geofísica, UNAM N103 "Analogías de sistemas hidrotermales fósiles (minería) y activos (geotermia)."

Acknowledgments

We thank the "Unidad de Equipamiento Científico" (MAINI), hosted at Universidad Católica del Norte, for their valuable support during scanning electron microscopy analysis. Furthermore, the authors are especially grateful to the "Laboratorio de Petrografía y Microtermometría" of the Instituto de Geofísica at the Universidad Nacional Autónoma de México for their support during this study.

Conflict of interest

The authors declare that the research was conducted in the absence of any commercial or financial relationships that could be construed as a potential conflict of interest.

Publisher's note

Supplementary material

The Supplementary Material for this article can be found online at: https://www.frontiersin.org/articles/10.3389/feart.2023.1197363/full#supplementary-material

References

Africano, F., and Bernard, A. (2000). Acid alteration in the fumarolic environment of Usu volcano, Hokkaido, Japan. *J. Volcanol. Geotherm. Res.* 97 (1-4), 475–495. doi:10.1016/s0377-0273(99)00162-6

Aguilera, F., Layana, S., Rodríguez-Díaz, A., González, C., Cortés, J., and Inostroza, M. (2016). Hydrothermal alteration, fumarolic deposits and fluids from Lastarria volcanic complex: A multidisciplinary study. *Andean Geol.* 43 (2), 166–169. doi:10.5027/andgeov43n2-a02

Aguilera, F. (2008). *Origen y naturaleza de los fluidos en los sistemas volcánicos, geotermales y termales de baja entalpía de la zona volcánica central (ZVC) entre los 17° 43's y 25° 10's*. Chile: Tesis de doctorado, Universidad Católica del Norte.

Aguilera, F., Tassi, F., Darrah, T., Moune, S., and Vaselli, O. (2012). Geochemical model of a magmatic–hydrothermal system at the Lastarria volcano, northern Chile. *Bull. Volcanol.* 74, 119–134. doi:10.1007/s00445-011-0489-5

Bacon, R. F., and Fanelli, R. (1943). The viscosity of sulfur1. *J. Am. Chem. Soc.* 65 (4), 639–648. doi:10.1021/ja01244a043

Balić-Žunić, T., Garavelli, A., Jakobsson, S. P., Jonasson, K., Katerinopoulos, A., Kyriakopoulos, K., et al. (2016). Fumarolic minerals: An overview of active European volcanoes. *Updat. Volcanology-From Volcano Model. Volcano Geol.*, 267–322. doi:10.5772/64129

Bennett, F. D., and Raccichini, S. M. (1978). Subaqueous sulphur lake in volcan poas. *Nature* 271 (5643), 342–344. doi:10.1038/271342a0

Calabrese, S., Aiuppa, A., Allard, P., Bagnato, E., Bellomo, S., Brusca, L., et al. (2011). Atmospheric sources and sinks of volcanogenic elements in a basaltic volcano (Etna, Italy). *Geochimica Cosmochimica Acta* 75 (23), 7401–7425. doi:10.1016/j.gca.2011.09.040

Colony, W. E., and Nordlie, B. E. (1973). Liquid sulfur at volcan azufre, Galapagos islands. *Econ. Geol.* 68 (3), 371–380. doi:10.2113/gsecongeo.68.3.371

Daga, R. B., Caselli, A. T., Ribeiro Guevara, S., and Agusto, M. R. (2017). Tefras emitidas durante la fase inicial hidromagmática (julio de 2012) del ciclo eruptivo 2012-actual (2016) del volcán Copahue (Andes del Sur) Asociación Geológica Argentina; Revista de la Asociación Geológica Argentina 74 (2), 191–206.

De Ronde, C. E. J., Chadwick, W. W., Ditchburn, R. G., Embley, R. W., Tunnicliffe, V., Baker, E. T., et al. (2015). Molten sulfur lakes of intraoceanic arc volcanoes. *Volcan. lakes* 1, 261–288. doi:10.1007/978-3-642-36833-2_11

Delmelle, P., Bernard, A., Kusakabe, M., Fischer, T. P., and Takano, B. (2000). Geochemistry of the magmatic–hydrothermal system of Kawah ijen volcano, east java, Indonesia. *J. Volcanol. Geotherm. Res.* 97 (1-4), 31–53. doi:10.1016/s0377-0273(99)00158-4

Delmelle, P., and Bernard, A. (2015). The remarkable chemistry of sulfur in hyper-acid crater lakes: A scientific tribute to bokuichiro Takano and minoru Kusakabe. *Volcan. lakes* 259, 239. doi:10.1007/978-3-642-36833-2_10

Delpino, D., and Bermúdez, A. (1993). "La actividad del volcán Copahue durante 1992," in *Erupción con emisiones de azufre piroclástico. Provincia de Neuquen, Argentina* (Mendoza, Argentina: XII Congreso Geológico Argentino), 292–301.

Edmonds, M., Mather, T. A., and Liu, E. J. (2018). A distinct metal fingerprint in arc volcanic emissions. *Nat. Geosci.* 11 (10), 790–794. doi:10.1038/s41561-018-0214-5

Embley, R. W., Baker, E. T., Butterfield, D. A., Chadwick, W. W., Lupton, J. E., Resing, J. A., et al. (2007). Exploring the submarine ring of fire: Mariana arc-western pacific. *Oceanography* 20 (4), 68–79. doi:10.5670/oceanog.2007.07

Fischer, T. P., Shuttleworth, S., and O'Day, P. A. (1998). Determination of trace and platinum-group elements in high ionic-strength volcanic fluids by sector-field inductively coupled plasma mass spectrometry (ICP-MS). *Fresenius' J. Anal. Chem.* 362, 457–464. doi:10.1007/s002160051106

Froger, J. L., Remy, D., Bonvalot, S., and Legrand, D. (2007). Two scales of inflation at Lastarria-Cordon del Azufre volcanic complex, central Andes, revealed from ASAR-ENVISAT interferometric data. *Earth Planet. Sci. Lett.* 255 (1-2), 148–163. doi:10.1016/j.epsl.2006.12.012

Giggenbach, W. F., and Matsuo, S. (1991). Evaluation of results from second and third IAVCEI field workshops on volcanic gases, Mt usu, Japan, and white island, New Zealand. *Appl. Geochem.* 6 (2), 125–141. doi:10.1016/0883-2927(91)90024-j

Giggenbach, W. F. (1987). Redox processes governing the chemistry of fumarolic gas discharges from White Island, New Zealand. *Appl. Geochem.* 2 (2), 143–161. doi:10.1016/0883-2927(87)90030-8

González, G., Mora-Amador, R., Ramírez, C., Rouwet, D., Alpizar, Y., Picado, C., et al. (2015). Historic activity and hazard analysis of Turrialba volcano, Costa Rica. *Rev. Geol. América Cent.* 52, 129–149. doi:10.15517/rgac.v0i52.19033

Greeley, R., Lee, S. W., Crown, D. A., and Lancaster, N. (1990). Observations of industrial sulfur flows: Implications for Io. *Icarus* 84 (2), 374–402. doi:10.1016/0019-1035(90)90045-b

Greeley, R., Theilig, E., and Christensen, P. (1984). The Mauna Loa sulfur flow as an analog to secondary sulfur flows (?) on Io. *Icarus* 60 (1), 189–199. doi:10.1016/0019-1035(84)90147-7

Harris, A., Carniel, R., Patrick, M., and Dehn, J. (2004). The sulfur flow fields of the Fossa di Vulcano. *Bull. Volcanol.* 66, 749–759. doi:10.1007/s00445-004-0361-y

Henderson, S. T., Delgado, F., Elliott, J., Pritchard, M. E., and Lundgren, P. R. (2017). Decelerating uplift at Lazufre volcanic center, Central Andes, from AD 2010 to 2016, and implications for geodetic models. *Geosphere* 13 (5), 1489–1505. doi:10.1130/ges01441.1

Hubberten, H. W., Nielsen, H., and Puchelt, H. (1975). The enrichment of 34S in the solfataras of the Nea Kameni volcano, Santorini archipelago, Greece. *Chem. Geol.* 16 (3), 197–205. doi:10.1016/0009-2541(75)90028-5

Ikehata, K., Date, M., Ishibashi, J. I., Kikugawa, G., and Mannen, K. (2019). Solid sulfur spherules near fumaroles of Hakone volcano, Japan. *Int. J. Earth Sci.* 108, 347–356. doi:10.1007/s00531-018-1657-z

Imai, N., Terashima, S., Itoh, S., and Ando, A. (1995). 1994 compilation of analytical data for minor and trace elements in seventeen GSJ geochemical reference samples Igneous rock series. *Geostand. Newsl.* 19 (2), 135–213. doi:10.1111/j.1751-908x.1995.tb00158.x

Inostroza, M., Aguilera, F., Menzies, A., Layana, S., González, C., Ureta, G., et al. (2020). Deposition of metals and metalloids in the fumarolic fields of Guallatiri and Lastarria volcanoes, northern Chile. *J. Volcanol. Geotherm. Res.* 393, 106803. doi:10.1016/j.jvolgeores.2020.106803

Kargel, J. S., Delmelle, P., and Nash, D. B. (1999). Volcanogenic sulfur on Earth and io: Composition and spectroscopy. *Icarus* 142 (1), 249–280. doi:10.1006/icar.1999.6183

Kusakabe, M., Komoda, Y., Takano, B., and Abiko, T. (2000). Sulfur isotopic effects in the disproportionation reaction of sulfur dioxide in hydrothermal fluids: Implications for the δ34S variations of dissolved bisulfate and elemental sulfur from active crater lakes. *J. Volcanol. Geotherm. Res.* 97 (1-4), 287–307. doi:10.1016/s0377-0273(99)00161-4

Layana, S., Aguilera, F., Inostroza, M., Tassi, F., Wilkes, T., Bredemeyer, S., et al. (2023). Evolution of the magmatic-hydrothermal system at Lastarria volcano (Northern Chile) between 2006 and 2019: Insights from fluid geochemistry. *Front. Earth Sci.* 11, 1. doi:10.3389/feart.2023.1114001

Leiding, B. (1936). Informe sobre las azufreras de Gorbea (the Sulphur mines at Gorbea). *Bol. Minas Pet.hile* 6 (60), 464–471.

Lopez, T., Aguilera, F., Tassi, F., De Moor, J. M., Bobrowski, N., Aiuppa, A., et al. (2018). New insights into the magmatic-hydrothermal system and volatile budget of Lastarria volcano, Chile: Integrated results from the 2014 IAVCEI CCVG 12th Volcanic Gas Workshop. *Geosphere* 14 (3), 983–1007. doi:10.1130/ges01495.1

MacKnight, W. J., and Tobolsky, A. V. (1965). in *Elemental sulfur*. Editor F. Bovey (New York: Interscience), 95.

Mambo, V. S., and Yoshida, M. (1993). Behavior of arsenic in volcanic gases. *Geochem. J.* 27 (4-5), 351–359. doi:10.2343/geochemj.27.351

Mandon, C. L., Seward, T. M., and Christenson, B. W. (2020). Volatile transport of metals and the Cu budget of the active White Island magmatic-hydrothermal system, New Zealand. *J. Volcanol. Geotherm. Res.* 398, 106905. doi:10.1016/j.jvolgeores.2020.106905

Matsushima, T., and Ono, K. (1959). Fundamental research on sulfur. VIII. On the viscosity of pure sulfur and the effect of selenium, arsenic, and carbonaceous organic substances. *Bull. Res. Inst. Min. Dress. Metall. Tohoku Univ.* 15, 5–10.

McFarlin, H., Thompson, G., McNutt, S. R., Braunmiller, J., and West, M. E. (2022). Classification of seismic activity at the Lazufre Volcanic System, based on 2011 to 2012 data. *Front. Earth Sci.* 1416, 1. doi:10.3389/feart.2022.890998

Meyer, B. (1976). Elemental sulfur. *Chem. Rev.* 76 (3), 367–388. doi:10.1021/cr60301a003

Mora-Amador, R. A., Rouwet, D., Vargas, P., and Oppenheimer, C. (2019). *The extraordinary sulfur volcanism of Poas from 1828 to 2018. Poás Volcano*. America: The Pulsing Heart of Central America Volcanic Zone, 45–78.

Moune, S., Gauthier, P. J., and Delmelle, P. (2010). Trace elements in the particulate phase of the plume of Masaya Volcano, Nicaragua. *J. Volcanol. Geotherm. Res.* 193 (3-4), 232–244. doi:10.1016/j.jvolgeores.2010.04.004

Naranjo, J. A. (1992). Chemistry and petrological evolution of the Lastarria volcanic complex in the north Chilean Andes. *Geol. Mag.* 129 (6), 723–740. doi:10.1017/s0016756800008451

Naranjo, J. A. (1988). Coladas de azufre de los volcanes Lastarria y Bayo en el norte d e Chile: Reología, génesis e importancia planetaria. *Rev. Geol. Chile* 31, 43–55.

Naranjo, J. A., and Cornejo, P. (1992). Hoja Salar de la Isla: Servicio Nacional de Geología y Minería, Carta Geológica de Chile 72. *scale* 1, 250.

Naranjo, J. A., and Francis, P. (1987). High velocity debris avalanche at Lastarria volcano in the north Chilean Andes. *Bull. Volcanol.* 49, 509–514. doi:10.1007/bf01245476

Naranjo, J. A. (2010). Geología del Complejo Volcánico Lastarria, Región de Antofagasta: Servicio Nacional de Geología y Minería, Carta Geológica de Chile 123. *scale* 1, 25.

Naranjo, J. A. (1985). Sulphur flows at Lastarria volcano in the north Chilean Andes. *Nature* 313 (6005), 778–780. doi:10.1038/313778a0

Oana, S., and Ishikawa, H. (1966). Sulfur isotopic fractionation between sulfur and sulfuric acid in the hydrothermal solution of sulfur dioxide. *Geochem. J.* 1 (1), 45–50. doi:10.2343/geochemj.1.45

Oelze, M., Frick, D. A., and Gleeson, S. A. (2021). Laser ablation split stream for *in situ* sulfur isotope and elemental analysis. *J. Anal. At. Spectrom.* 36, 1118–1124. doi:10.1039/d1ja00083g

Ohmoto, H., and Lasaga, A. C. (1982). Kinetics of reactions between aqueous sulfates and sulfides in hydrothermal systems. *Geochimica Cosmochimica Acta* 46 (10), 1727–1745. doi:10.1016/0016-7037(82)90113-2

Olmez, I., Finnegan, D. L., and Zoller, W. H. (1986). Iridium emissions from Kilauea volcano. *J. Geophys. Res. Solid Earth* 91 (B1), 653–663. doi:10.1029/jb091ib01p00653

Oppenheimer, C., and Stevenson, D. (1989). Liquid sulphur lakes at Poás volcano. *Nature* 342 (6251), 790–793. doi:10.1038/342790a0

Oppenheimer, C. (1992). Sulphur eruptions at volcán Poás, Costa Rica. *J. Volcanol. Geotherm. Res.* 49 (1-2), 1–21. doi:10.1016/0377-0273(92)90002-u

Piochi, M., Mormone, A., Balassone, G., Strauss, H., Troise, C., and De Natale, G. (2015). Native sulfur, sulfates and sulfides from the active Campi Flegrei volcano (southern Italy): Genetic environments and degassing dynamics revealed by mineralogy and isotope geochemistry. *J. Volcanol. Geotherm. Res.* 304, 180–193. doi:10.1016/j.jvolgeores.2015.08.017

Pritchard, M. E., and Simons, M. (2002). A satellite geodetic survey of large-scale deformation of volcanic centres in the central Andes. *Nature* 418 (6894), 167–171. doi:10.1038/nature00872

Pritchard, M. E., and Simons, M. (2004). An InSAR-based survey of volcanic deformation in the central Andes. *Geochem. Geophys. Geosystems* 5 (2). doi:10.1029/2003gc000610

Robidoux, P., Rizzo, A. L., Aguilera, F., Aiuppa, A., Artale, M., Liuzzo, M., et al. (2020). Petrological and noble gas features of Lascar and Lastarria volcanoes (Chile): Inferences on plumbing systems and mantle characteristics. *Lithos* 370, 105615. doi:10.1016/j.lithos.2020.105615

Rodríguez, I., Páez, J., de Vries, M. S. V. W., de Vries, B. V. W., and Godoy, B. (2020). Dynamics and physical parameters of the Lastarria debris avalanche, Central Andes. *J. Volcanol. Geotherm. Res.* 402, 106990. doi:10.1016/j.jvolgeores.2020.106990

Rodríguez, M. (1962). *La minería del azufre en Chile*. USA: Ministerio de Minería, Servicio de Minas del Estado de Chile, 41p.

Romer, R. L., and Hahne, K. (2010). Life of the rheic ocean: Scrolling through the shale record. *Gondwana Res.* 17 (2-3), 236–253. doi:10.1016/j.gr.2009.09.004

Rouwet, D., Mora-Amador, R., Ramirez, C., Gonzalez, G., Baldoni, E., Pecoraino, G., et al. (2021). Response of a hydrothermal system to escalating phreatic unrest: The case of Turrialba and irazú in Costa Rica (2007–2012). *Earth, Planets Space* 73, 142–226. doi:10.1186/s40623-021-01471-8

Rouwet, D., Mora-Amador, R., Ramírez, C., González, G., and Inguaggiato, S. (2017). Dynamic fluid recycling at Laguna Caliente (Poás, Costa Rica) before and during the 2006–ongoing phreatic eruption cycle (2005–10). *Geol. Soc. Lond. Spec. Publ.* 437 (1), 73–96. doi:10.1144/sp437.11

Rowe, G. L., Jr (1994). Oxygen, hydrogen, and sulfur isotope systematics of the crater lake system of Poas volcano, Costa Rica. *Geochem. J.* 28 (3), 263–287. doi:10.2343/geochemj.28.263

Rubero, P. A. (1964). Effect of hydrogen sulfide on the viscosity of sulfur. *J. Chem. Eng. Data* 9 (4), 481–484. doi:10.1021/je60023a001

Ruch, J., Anderssohn, J., Walter, T. R., and Motagh, M. (2008). Caldera-scale inflation of the Lazufre volcanic area, south America: Evidence from InSAR. *J. Volcanol. Geotherm. Res.* 174 (4), 337–344. doi:10.1016/j.jvolgeores.2008.03.009

Salvage, R. O., Avard, G., de Moor, J. M., Pacheco, J. F., Brenes Marin, J., Cascante, M., et al. (2018). Renewed explosive phreatomagmatic activity at Poás volcano, Costa Rica in April 2017. *Front. Earth Sci.* 6, 160. doi:10.3389/feart.2018.00160

Scolamacchia, T., and Cronin, S. J. (2016). Idiosyncrasies of volcanic sulfur viscosity and the triggering of unheralded volcanic eruptions. *Front. Earth Sci.* 4, 24. doi:10.3389/feart.2016.00024

Skinner, B. J. (1970). A sulfur lava flow on Mauna Loa. *Pac. Sci.* 24, 144–145.

Spica, Z., Legrand, D., Iglesias, A., Walter, T. R., Heimann, S., Dahm, T., et al. (2015). Hydrothermal and magmatic reservoirs at Lazufre volcanic area, revealed by a high-resolution seismic noise tomography. *Earth Planet. Sci. Lett.* 421, 27–38. doi:10.1016/j.epsl.2015.03.042

Steudel, R., and Eckert, B. (2003). Solid sulfur allotropes. *Elem. sulfur sulfur-rich Compd.* I, 1–80. doi:10.1007/b12110

Stoiber, R. E., and Rose, W. I., Jr (1974). Fumarole incrustations at active Central American volcanoes. *Geochimica Cosmochimica Acta* 38 (4), 495–516. doi:10.1016/0016-7037(74)90037-4

Symonds, R. B., Reed, M. H., and Rose, W. I. (1992). Origin, speciation, and fluxes of trace-element gases at Augustine volcano, Alaska: Insights into magma degassing and fumarolic processes. *Geochimica Cosmochimica Acta* 56 (2), 633–657. doi:10.1016/0016-7037(92)90087-y

Symonds, R. B., Rose, W. I., Reed, M. H., Lichte, F. E., and Finnegan, D. L. (1987). Volatilization, transport and sublimation of metallic and non-metallic elements in high temperature gases at Merapi Volcano, Indonesia. *Geochimica Cosmochimica Acta* 51 (8), 2083–2101. doi:10.1016/0016-7037(87)90258-4

Takano, B., Saitoh, H., and Takano, E. (1994). Geochemical implications of subaqueous molten sulfur at Yugama crater lake, Kusatsu-Shirane volcano, Japan. *Geochem. J.* 28 (3), 199–216. doi:10.2343/geochemj.28.199

Takano, B., and Watanuki, K. (1990). Monitoring of volcanic eruptions at Yugama crater lake by aqueous sulfur oxyanions. *J. Volcanol. Geotherm. Res.* 40 (1), 71–87. doi:10.1016/0377-0273(90)90107-q

Tamburello, G., Hansteen, T. H., Bredemeyer, S., Aiuppa, A., and Tassi, F. (2014). Gas emissions from five volcanoes in northern Chile and implications for the volatiles budget of the Central Volcanic Zone. *Geophys. Res. Lett.* 41 (14), 4961–4969. doi:10.1002/2014gl060653

Theilig, E. (1982). *A primer on sulfur for the planetary geologist (No. NASA-CR-3594)*. Germany: NASA.

Touro, F. J., and Wiewiorowski, T. K. (1966). Viscosity—chain length relationship in molten sulfur systems. *J. Phys. Chem.* 70 (1), 239–241. doi:10.1021/j100873a040

Trumbull, R. B., Wittenbrink, R., Hahne, K., Emmermann, R., Büsch, W., Gerstenberger, H., et al. (1999). Evidence for Late Miocene to Recent contamination of arc andesites by crustal melts in the Chilean Andes (25–26 S) and its geodynamic implications. *J. S. Am. Earth Sci.* 12 (2), 135–155. doi:10.1016/s0895-9811(99)00011-5

Ueda, A., Sakai, H., and Sasaki, A. (1979). Isotopic composition of volcanic native sulfur from Japan. *Geochem. J.* 13 (6), 269–275. doi:10.2343/geochemj.13.269

Varrica, D., Aiuppa, A., and Dongarrà, G. (2000). Volcanic and anthropogenic contribution to heavy metal content in lichens from Mt. Etna and Vulcano island (Sicily). *Environ. Pollut.* 108 (2), 153–162. doi:10.1016/s0269-7491(99)00246-8

Watanabe, T. (1940). Eruption of molten sulphur from siretoko-iosan volcano, hokkaido, Japan. *Jpn. J. Geol. Geogr.* 17, 289–310.

Watanabe, T., and Shimotomai, T. (1937). Volcanic activity of Shiretokoiozan, Kitaminokuni. 1936, Bulletin of Hokkaido Geological Survey 9, 37. (in Japanese; the Japanese title "Kitaminokuni Shiretokoiozan showajuichinenno katsudou. Hokkaido Chishitsu Chosakai Hokoku 9" is translated by Dr. Mutsunori Yamamoto).

Xu, Y., Schoonen, M. A. A., Nordstrom, D. K., Cunningham, K. M., and Ball, J. W. (2000). Sulfur geochemistry of hydrothermal waters in Yellowstone National Park, Wyoming, USA. II. Formation and decomposition of thiosulfate and polythionate in Cinder Pool. *J. Volcanol. Geotherm. Res.* 97 (1-4), 407–423. doi:10.1016/s0377-0273(99)00173-0

Yamamoto, M., Goto, T. N., and Kiji, M. (2017). Possible mechanism of molten sulfur eruption: Implications from near-surface structures around of a crater on a flank of Mt. Shiretokoiozan, Hokkaido, Japan. *J. Volcanol. Geotherm. Res.* 346, 212–222. doi:10.1016/j.jvolgeores.2017.11.009

Zoller, W. H., Gladney, E. S., and Duce, R. A. (1974). Atmospheric concentrations and sources of trace metals at the South Pole. *science* 183 (4121), 198–200. doi:10.1126/science.183.4121.198

Zoller, W. H., Parrington, J. R., and Phelan Kotra, J. M. (1983). Iridium enrichment in airborne particles from Kilauea volcano: January 1983. *Science* 222 (4628), 1118–1121. doi:10.1126/science.222.4628.1118